Journal of
Translational Medicine

RESEARCH

Open Access

AC099850.3 promotes HBV-HCC cell proliferation and invasion through regulating CD276: a novel strategy for sorafenib and immune checkpoint combination therapy

Aoxiao He[1†], Zhihao Huang[1†], Qian Feng[2], Shan Zhang[3], Fan Li[4], Dan Li[4], Hongcheng Lu[1*] and Jiakun Wang[1*]

Abstract

Background This study investigates the molecular mechanisms of CC@AC&SF@PP NPs loaded with AC099850.3 siRNA and sorafenib (SF) for improving hepatitis B virus-related hepatocellular carcinoma (HBV-HCC).

Methods A dataset of 44 HBV-HCC patients and their survival information was selected from the TCGA database. Immune genes related to survival status were identified using the ImmPort database and WGCNA analysis. A prognostic risk model was constructed and analyzed using Lasso regression. Differential analysis was performed to screen key genes, and their significance and predictive accuracy for HBV-HCC were validated using Kaplan–Meier survival curves, ROC analysis, CIBERSORT analysis, and correlation analysis. The correlation between AC099850.3 and the gene expression matrix was calculated, followed by GO and KEGG enrichment analysis using AC099850.3 and its co-expressed genes. HepG2.2.15 cells were selected for in vitro validation, and lentivirus interference, cell cycle determination, CCK-8 experiments, colony formation assays, Transwell experiments, scratch experiments, and flow cytometry were performed to investigate the effects of key genes on HepG2.2.15 cells. A subcutaneous transplanted tumor model in mice was constructed to verify the inhibitory effect of key genes on HBV-HCC tumors. Subsequently, pH-triggered drug release NPs (CC@AC&SF@PP) were prepared, and their therapeutic effects on HBV-HCC in situ tumor mice were studied.

Results A prognostic risk model (AC012313.9, MIR210HG, AC099850.3, AL645933.2, C6orf223, GDF10) was constructed through bioinformatics analysis, showing good sensitivity and specificity in diagnostic prediction. AC099850.3 was identified as a key gene, and enrichment analysis revealed its impact on cell cycle pathways. In vitro cell experiments demonstrated that AC099850.3 promotes HepG2.2.15 cell proliferation and invasion by regulating immune checkpoint CD276 expression and cell cycle progression. In vivo, subcutaneously transplanted tumor experiments showed that AC099850.3 promotes the growth of HBV-HCC tumors in nude mice. Furthermore, pH-triggered drug release NPs (CC@AC&SF@PP) loaded with AC099850.3 siRNA and SF were successfully prepared and delivered to the in situ HBV-HCC, enhancing the effectiveness of combined therapy for HBV-HCC.

---

†Aoxiao He and Zhihao Huang are co-first authors.

*Correspondence:
Hongcheng Lu
fatlam@buaa.edu.cn
Jiakun Wang
417037196@qq.com
Full list of author information is available at the end of the article

He *et al. Journal of Translational Medicine*   (2024) 22:809

Page 2 of 26

Conclusions AC099850.3 accelerates the cell cycle progression and promotes the occurrence and development of HBV-HCC by upregulating immune checkpoint CD276 expression. CC@AC&SF@PP NPs loaded with AC099850.3 siRNA and SF improve the effectiveness of combined therapy for HBV-HCC.

Keywords Hepatitis B virus-related hepatocellular carcinoma, AC099850.3, CD276, Cell cycle, Cell proliferation and invasion, Nanoparticles, Combined therapy, Sorafenib

Introduction

Hepatitis B virus-related hepatocellular carcinoma (HBV-HCC) is a serious disease that poses a significant threat to human health, with a high incidence and mortality rate worldwide [1, 2]. Although there are currently some treatment methods available for managing HBV-HCC, their effectiveness remains suboptimal [3]. Therefore, further research on the molecular mechanisms of HBV-HCC and the development of new treatment strategies are needed to improve therapeutic outcomes.

The long non-coding RNA (lncRNA) AC099850.3 has attracted widespread attention in cancer research in recent years. AC099850.3 is involved in multiple biological processes such as cell proliferation, apoptosis, migration, and invasion by regulating the expression of target genes. Studies have shown that AC099850.3 exhibits abnormal expression in various cancers, particularly in lung cancer [4, 5]. High expression of AC099850.3 is associated with the aggressiveness of tumors and poor prognosis. For instance, AC099850.3 promotes cancer cell proliferation and migration by competitively binding to miRNA, thereby relieving its inhibitory effect on target genes. Therefore, AC099850.3 is considered a potential therapeutic target, and its role in cancer has become a research focus.

CD276, also known as B7-H3, is a type I transmembrane protein that belongs to the B7 family of immune regulatory molecules. Functioning as an immune checkpoint molecule, CD276 plays a crucial role in immune evasion and the tumor immune microenvironment. By binding to its receptors, CD276 inhibits the activation and proliferation of T cells, thereby suppressing the immune system's recognition and killing ability against tumor cells [6]. High expression of CD276 is associated with poor prognosis and increased tumor invasiveness in various cancers [7, 8]. Consequently, immunotherapeutic strategies targeting CD276, such as anti-CD276 antibodies and CD276-directed CAR-T cell therapy, have emerged as important directions in cancer research.

As a novel treatment strategy, nanomedicine delivery systems have shown tremendous potential in cancer treatment [9–12]. This system utilizes NPs as carriers to deliver drugs, enhancing their targeting specificity in tumor tissue and reducing side effects in non-tumor tissue [9, 13–15]. The constrained and deactivated model (AC&SF) NPs represent a novel nanomedicine delivery carrier with biocompatibility and good in vitro regenerative properties.

In the treatment of HBV-HCC, AC099850.3 is considered an important regulatory factor playing a crucial role in the cell cycle progression [16–18]. Recent studies have revealed that AC099850.3 promotes the occurrence and development of HBV-HCC by regulating the expression of immune checkpoint CD276 and facilitating cell cycle progression [19]. In order to gain a deeper understanding of the functions and potential therapeutic value of AC099850.3, further research is required to investigate its mechanism of action in HBV-HCC [5, 20].

Sorafenib (SF) is the first drug approved by the Food and Drug Administration (FDA) for the treatment of advanced HCC and remains one of the most commonly used drugs in systemic therapy for hepatocellular carcinoma. It is an effective targeted chemotherapy drug that can inhibit angiogenesis, proliferation, and invasion [21, 22]. However, due to its poor solubility and potential for various adverse reactions such as hypertension, diarrhea, hand-foot syndrome, and rash/desquamation, the use of SF as a monotherapy is significantly restricted in clinical applications [23–25]. Therefore, there is an urgent need to develop new treatment strategies.

The occurrence and metastasis of HCC involve a complex process characterized by multiple genes, factors, and steps [26]. Gene therapy holds promise for achieving positive treatment outcomes. Moreover, an increasing body of evidence supports the synergistic therapeutic effect of combining gene therapy with chemotherapy for HCC [27, 28]. The combination therapy of PD-1 or PD-L1 with SF has demonstrated significant synergistic therapeutic effects in treating HCC [29, 30], making it a promising and potent therapeutic approach.

The objective of this study was to investigate the effectiveness of AC099850.3 siRNA and SF in combination therapy for HBV-HCC and elucidate its molecular mechanisms. We hypothesize that AC099850.3 may promote tumor proliferation and invasion by upregulating CD276, thus driving the progression of HBV-HCC. Furthermore, we propose that combining siRNA targeting AC099850.3 with SF may offer a novel therapeutic strategy for the treatment of HBV-HCC. Initially, we screened a dataset and survival information of HBV-HCC patients from the

He *et al. Journal of Translational Medicine*   (2024) 22:809

Page 3 of 26

TCGA database. Through analysis using the ImmPort database and WGCNA, we identified immune gene modules associated with the survival status of HBV-HCC [31–33]. Subsequently, we employed differential analysis to further identify key genes related to HBV-HCC [34]. In vitro experiments and a subcutaneous transplanted tumor model in mice were then used to study the role of AC099850.3 in HBV-HCC cell proliferation and invasion, as well as assess its impact on tumor growth [4, 35, 36].

The significance of this study lies in gaining a deeper understanding of the mechanisms by which AC099850.3 functions in the occurrence and progression of HBV-HCC, providing new targets and strategies for its treatment. Moreover, we prepared pH-triggered drug-delivery NPs (CC@AC&SF@PP) and studied their therapeutic effects on HBV-HCC tumors. We believe that the results of this research will offer new insights and approaches for the clinical treatment of HBV-HCC, serving as a reference for further studies and translational applications in this field.

Results

Prognostic model based on immune-related genes demonstrates good diagnostic predictive value in HBV-HCC

Firstly, we obtained liver cancer RNA-Seq (TCGA-LIHC) data from the TCGA database. Based on the characteristic of HBV positivity in clinical data of LIHC patients, we extracted HBV-HCC RNA-Seq data comprising 50 normal samples and 44 tumor samples. The genes in the expression matrix were categorized into mRNA (19,574 genes) and lncRNA (14,056 genes), and their expression matrix, survival information, and clinical information were merged. Clustering of all samples and selection of the optimal soft threshold was performed to construct gene modules based on the merged mRNA matrix (Figure S1A-B), resulting in the construction of the WGCNA co-expression network. Through the co-expression network, all genes were divided into seven different gene modules (Figure S1C), and heat map results of dynamic splice variation analysis were obtained, showing correlations with patient survival time, survival status, age, gender, grading, and staging (Fig. 1A). The MEbrown module, with the highest correlation with survival status, was selected for further analysis. This module consisted of 174 genes (Table S1), with a correlation of r=0.31 (P=0.04) to HBV-HCC. Subsequently, we downloaded immune-related gene sets from the ImmPort database (Table S2) and extracted immune-related mRNAs from the MEbrown module. In addition, we screened lncRNAs that were correlated with immune-related mRNAs in the MEbrown module (Table S3).

Next, we performed a single-variable Cox regression analysis using the "survival" package to screen for immune-related mRNAs (22 genes) and lncRNAs (36 genes) associated with prognosis (Table S4). LASSO analysis was then conducted to draw Lasso regression coefficient plots and cross-validation plots (Fig. 1B, Figure S1D), further narrowing down the candidate gene list to select six model genes with the best lambda values: AC012313.9, MIR210HG, AC099850.3, AL645933.2, C6orf223, and GDF10. Patients were divided into low-risk and high-risk subgroups based on the median risk score, and the differential expression of the six model genes between the high and low-risk groups was demonstrated, showing significant differences for all six model genes (Fig. 1C). Univariate and multivariate Cox regression analyses were conducted to assess whether the risk score could serve as an independent prognostic factor. The results showed that the risk score was significantly associated with overall survival (OS) and could be an independent prognostic factor (Fig. 1D, E). KM survival analysis was performed on randomized subsets of the dataset (train), test subsets (test), and the entire dataset (all), demonstrating that low-risk HBV-HCC had a significantly better prognosis than high-risk HBV-HCC (P < 0.001, P = 0.031, and P < 0.001) (Fig. 1F, Figure S1E-F). ROC curve analysis showed that the model had a high diagnostic predictive value for HBV-HCC (AUC=0.873, 0.729, 0.984) (Fig. 1G, Figure S2A-B). Setting the median risk score as the threshold and plotting the survival status graph demonstrated that the majority of high-risk HBV-HCC patients died, further proving the stability of the model (Fig. 1H, Figure S2C, E). Heat maps showed the expression patterns of the six model genes in low-risk and high-risk HBV-HCC, and consistent trends were observed in the train and test subsets (Fig. 1I, Figure S2D, F).

In conclusion, the prognostic model constructed based on immune-related genes (AC012313.9, MIR210HG, AC850.3, AL645933.2, C6orf223, GDF10) demonstrated good sensitivity and specificity, with high diagnostic predictive value for HBV-HCC.

AC099850.3 is a key gene in HBV-HCC and plays an important role in tumor immunotherapy

In order to further identify key genes in HBV-HCC, we conducted differential analysis on 50 normal samples and 44 tumor samples (Fig. 2A, B). We found significant differences in the genes MIR210HG (logFC=0.33), AC099850.3 (logFC=1.33), AL645933.2 (logFC=0.06), and C6orf223 (logFC=0.78), while AC012313.9 and GDF10 showed no differences (Fig. 2C, Figure S3A-E). We selected AC099850.3, which had the highest expression level, as the key gene for further investigation in
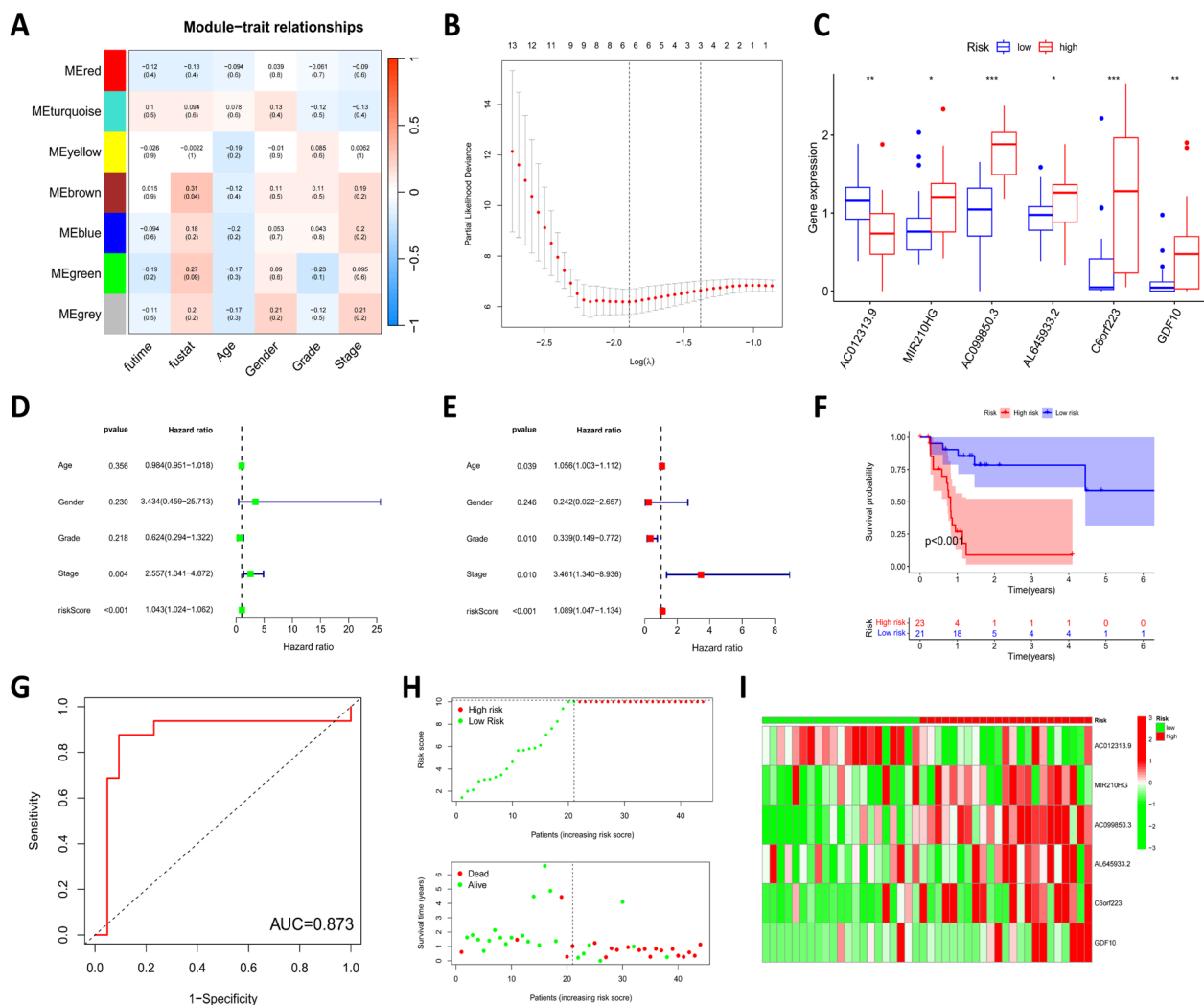
He *et al. Journal of Translational Medicine* (2024) 22:809

Page 4 of 26

Fig. 1 Construction and validation of the HBV-HCC prognostic model. **A** Heatmap depicting the correlation between gene modules and patient survival time, survival status, age, gender, grade, and stage; **B** Results of LASSO analysis, where the x-axis represents log(λ) values, the y-axis represents Partial Likelihood Deviance, the top portion represents the number of genes retained for a corresponding log(λ) value used in the calculation, the dashed line represents the log(λ) value and number of retained genes at the optimal Partial Likelihood Deviance; **C** Differential expression levels of the six model genes between high and low-risk groups; **D** Risk score evaluation using univariate Cox regression analysis; **E** Risk score evaluation using multivariate Cox regression analysis, with Hazard ratio indicating the risk rate, a Hazard ratio greater than 1 signifies high risk, while a Hazard ratio less than 1 signifies low risk; **F** Kaplan–Meier survival curves for the high and low-risk groups; **G** ROC curve analysis indicating the predictive value of the high and low-risk groups in HBV-HCC diagnosis; **H** Risk curves and patient survival status graphs for the high and low-risk groups; **I** Heatmap displaying the expression levels of the six model genes in the high and low-risk groups; high-risk group: 23 samples; low-risk group: 21 samples; * denotes comparison between high and low-risk groups, P < 0.05; ** denotes comparison between high and low-risk groups, P < 0.01; *** denotes comparison between high and low-risk groups, P < 0.001

HBV-HCC. Additionally, there was a significant difference in AC099850.3 expression in paired samples (Fig. 2D). Following this, we divided the 44 tumor samples into high and low-expression groups based on the median expression level of AC099850.3 and performed KM survival analysis, which revealed that the prognosis of HBV-HCC in the low-expression group was significantly better than that in the high-risk group (P = 0.007)

(Fig. 2E). ROC curve analysis showed that the AUC for 1-year, 3-year, and 5-year survival was 0.836, 0.847, and 0.826, respectively, indicating the stable predictive ability of AC099850.3 (Fig. 2F).

By using the CIBERSORT algorithm to analyze the differential composition of immune cells in HBV-HCC patient samples, we found significant differences in the immune cell components CD8 T cells and follicular
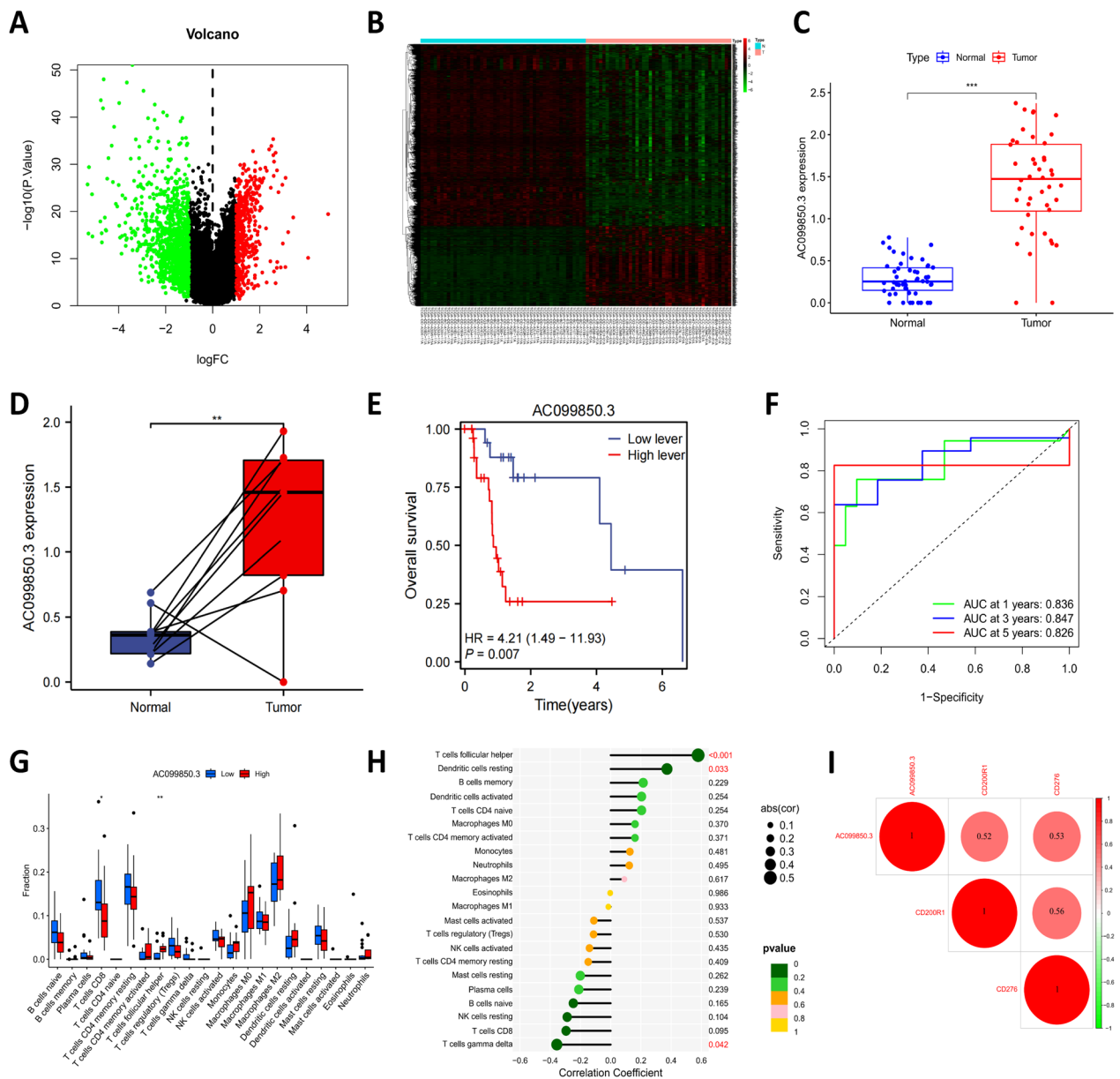
He *et al. Journal of Translational Medicine*   (2024) 22:809

Page 5 of 26

Fig. 2 Screening and validation of key genes in HBV-HCC. **A**, **B** Volcano plot and heatmap of differentially expressed genes between 50 normal samples and 44 HBV-HCC samples from the TCGA database (red dots represent upregulated genes, green dots represent downregulated genes, black dots represent genes with no significant difference in expression between the two groups); **C** Differential expression level of AC099850.3 gene between 50 normal samples and 44 HBV-HCC samples; **D** Differential expression level of AC099850.3 gene between 8 HBV-HCC samples and their paired normal samples in the TCGA database; **E** Kaplan–Meier survival curve of AC099850.3 high and low expression groups; **F** ROC curve analysis of the predictive value of the AC099850.3 high and low expression groups in HBV-HCC diagnosis; **G** Analysis of the differences in immune cell composition between AC099850.3 high and low expression groups, where the x-axis represents immune cell types and the y-axis represents the proportion of immune cells in the samples, with blue representing the low expression group of AC099850.3 and red representing the high expression group of AC099850.3; **H** Lollipop plot illustrating the correlation between significantly different immune cell components and AC099850.3 expression levels; **I** Heatmap showing the correlation between AC099850.3 and immune checkpoints; * denotes comparison between the two groups, P < 0.05; ** denotes comparison between the two groups, P < 0.01; *** denotes comparison between the two groups, P < 0.001

He *et al. Journal of Translational Medicine*   (2024) 22:809

Page 6 of 26

helper T cells (Fig. 2G). Furthermore, correlation analysis between all immune cell components and AC099850.3 expression revealed significant correlations between inactive dendritic cells (R = 0.37, P = 0.033), follicular helper T cells (R = 0.58, P < 0.001), and T cells γδ (R = -0.36, P = 0.042) and the expression of AC099850.3 (Fig. 2H, Figure S3F-H). In addition, we investigated the correlation between AC099850.3 and immune checkpoints and found significant correlations with CD200R1 (R = 0.52, P < 0.001) and CD276 (R = 0.53, P < 0.001) (Fig. 2I). The study on the correlation between AC099850.3 and tumor mutation burden showed a positive correlation between AC099850.3 expression and tumor mutation burden (R = 0.34, P = 0.026) (Figure S3I).

These results indicate that AC099850.3 is a key gene in HBV-HCC, which plays an important role in tumor immunotherapy by influencing immune cell infiltration and the expression of immune checkpoint factors.

Regulation of nuclear division and cell cycle by AC099850.3 and its co-expressed genes in HBV-HCC

To explore the function of AC099850.3 in HBV-HCC, we selected 727 HBV-HCC genes that were co-expressed with AC099850.3, using a correlation threshold of greater than 0.7 and P < 0.001 (Table S5). The circle plot and correlation scatter plot depicted the top-ranking genes correlated with AC099850.3 (Fig. 3A and Figure S4). We performed GO functional analysis and KEGG pathway analysis on AC099850.3 and its co-expressed genes.

GO functional analysis revealed that AC099850.3 and its co-expressed genes were primarily enriched in BP, such as mitotic nuclear division, positive regulation of cell cycle, chromosome segregation, DNA-templated DNA replication, and mitotic sister chromatid segregation. In terms of CC, the enrichment was observed in microtubules, chromosomal regions, nuclear chromosomes, condensed chromosomes, and centromeric regions. Moreover, in MF, enrichment was observed in ATP hydrolysis activity, catalytic activity acting on DNA, helicase activity, microtubule motor activity, and single-stranded DNA binding (Fig. 3B, C). KEGG pathway analysis revealed that AC099850.3 and its co-expressed genes were mainly enriched in Motor proteins and Cell cycle pathways (Fig. 3D).

These functional enrichment results suggest that AC099850.3 and its co-expressed genes are primarily involved in the positive regulation of nuclear division and the cell cycle and chromosome separation and are enriched in structures such as microtubules, chromosomal regions, and centromeres. In terms of molecular functions, they are mainly involved in ATP hydrolysis activity, helicase activity, and microtubule motor activity. According to KEGG analysis, AC099850.3 and its co-expressed genes are enriched in the cell cycle pathway (ID: hsa04110, P < 0.001). Previous studies have demonstrated that genes related to cell cycle regulation may be associated with tumor occurrence, development, and metastasis [37]. Additionally, the literature suggests a close association between LncRNA AC099850.3 and proliferation and invasion of HCC and its correlation with patient prognosis [20], which is consistent with our findings.

Based on the above results, we speculate that AC099850.3 promotes tumor cell proliferation and invasion in HBV-HCC by influencing the cell cycle, thus participating in the occurrence and development of this cancer.

AC099850.3 regulates cell cycle progression and proliferation and invasion of HepG2.2.15 cells through modulation of CD276

Immunotherapy has emerged as a primary approach for cancer treatment. In investigating the proliferative effects of immune checkpoints in different tumors, the role of CD276 (B7-H3) in regulating cell cycle and tumor proliferation has been identified [38, 39]. Through bioinformatics analysis, a positive correlation between AC099850.3 and immune checkpoint CD276 was observed (Fig. 2I). Therefore, we hypothesized that AC099850.3 may influence cell cycle progression and promote the proliferation and invasion of HepG2.2.15 cells by modulating the expression of immune checkpoint CD276.

To validate our hypothesis, we transfected HepG2.2.15 cells with si-NC, si-AC099850.3, si-CD276 and confirmed transfection efficiency via qRT-PCR. We proceeded with subsequent experiments using the group exhibiting the most effective silencing efficiency (Fig. 4A). In the cell cycle experiment conducted after 48 h (Fig. 4B), the proportion of HepG2.2.15 cells in the G2/M phase increased significantly in the si-AC099850.3 and si-CD276 group, indicating a G2/M phase cell cycle arrest compared to the si-NC group. Furthermore, compared to the si-AC099850.3 + oe-NC group, the si-AC099850.3 + oe-CD276 group showed a decrease in the proportion of HepG2.2.15 cells in the G2/M phase, alleviating the G2/M phase cell cycle arrest.

Cell proliferation ability was assessed using CCK-8 and colony formation assay, and the results showed (Fig. 4C, D) a significant reduction in the proliferation ability of HepG2.2.15 cells in the si-AC099850.3 and si-CD276 group when compared to the si-NC group. In contrast, the si-AC099850.3 + oe-CD276 group exhibited a significant enhancement in cell proliferation ability compared to the si-AC099850.3 + oe-NC group. Flow cytometry analysis of cell apoptosis (Fig. 4E) revealed increased apoptosis in HepG2.2.15 cells in the si-AC099850.3 and

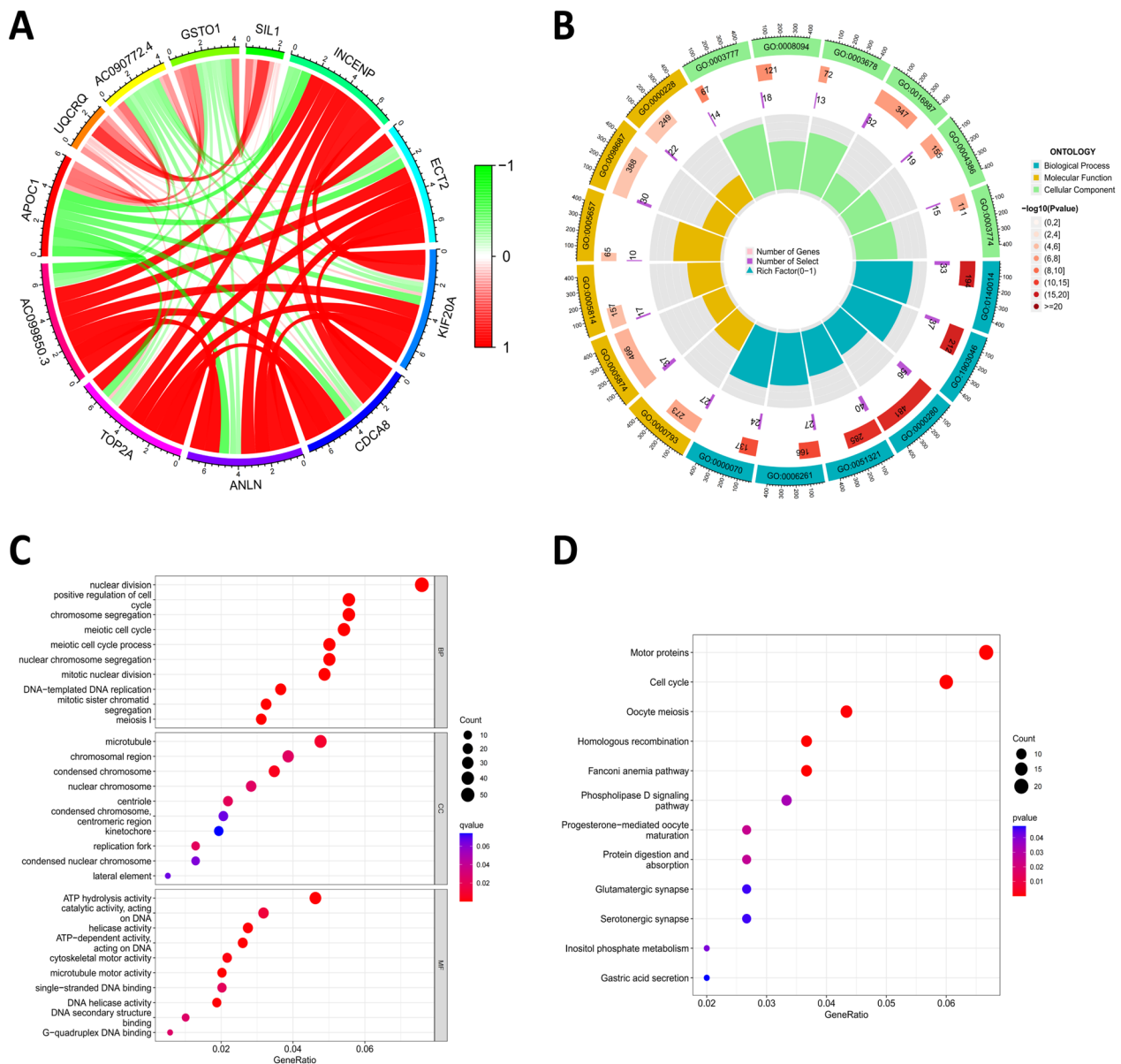He *et al. Journal of Translational Medicine*   (2024) 22:809

Page 7 of 26

Fig. 3 Functional enrichment analysis of AC099850.3 and its co-expressed genes. **A** Circos plot displaying the top-ranked genes correlated with AC099850.3; **B**, **C** Circos plot and bubble plot, illustrating the GO functional analysis of AC099850.3 and its co-expressed genes at the BP, CC, and MF levels; **D** Bubble plot depicting the KEGG pathway enrichment analysis of AC099850.3 and its co-expressed genes, where the size of the dots represents the number of selected genes and the color represents the P-value of the enrichment analysis

(See figure on next page.)

Fig. 4 Impact of AC099850.3/CD276 expression on HepG2.2.15 cells. **A** qRT-PCR assessing the transfection efficiency of three AC099850.3 siRNAs and three CD276 siRNAs in HepG2.2.15 cells; **B** Flow cytometry determining the cell cycle and presenting a bar graph of cell proportions in different phases of the cell cycle; **C**, **D** CCK-8 assay and colony formation assay evaluating the proliferation ability of the different cell groups; **E** Flow cytometry measuring the apoptosis of the different cell groups; **F**, **G** Scratch assay (Scale bar: 100 μm) and Transwell assay (Scale bar: 50 μm) examining the migration and invasion capabilities of the different cell groups; **H** Western blot analysis assessing the expression levels of CD276, E-cadherin, N-cadherin, and Vimentin in HepG2.2.15 cells; * denotes comparison with the si-NC group, $P < 0.05$; ** denotes comparison with the si-NC group, $P < 0.01$; *** denotes comparison with the si-NC group, $P < 0.001$; # denotes comparison with the si-AC099850.3 + oe-NC group, $P < 0.05$; ## denotes comparison with the si-AC099850.3 + oe-NC group, $P < 0.01$; ### denotes comparison with the si-AC099850.3 + oe-NC group, $P < 0.001$; all cell experiments were repeated three times
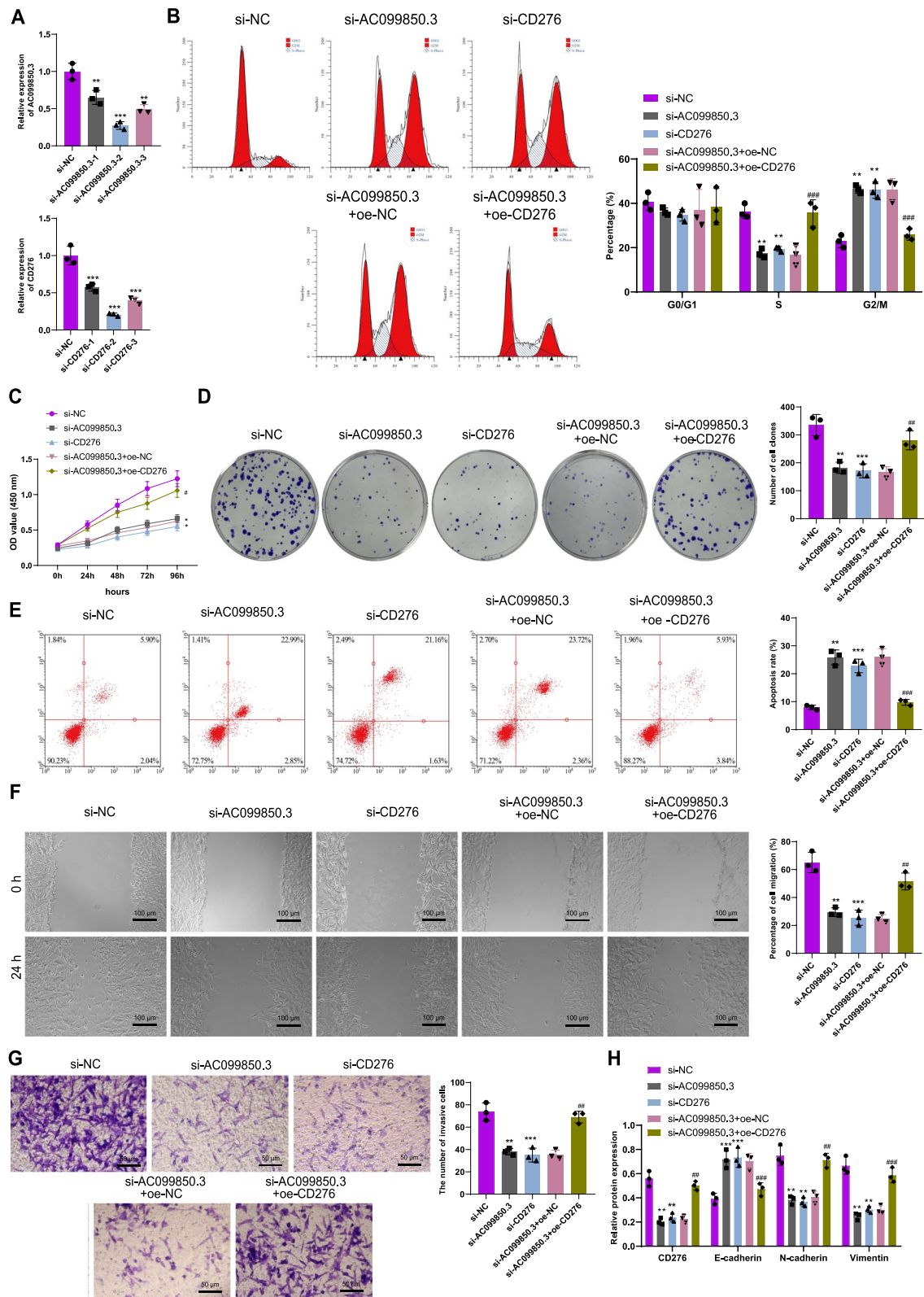
He *et al. Journal of Translational Medicine*   (2024) 22:809

Page 8 of 26

Fig. 4 (See legend on previous page.)

He *et al. Journal of Translational Medicine* (2024) 22:809

Page 9 of 26

si-CD276 groups compared to the si-NC group. Conversely, the si-AC099850.3 + oe-CD276 group demonstrated a reduction in apoptosis compared to the si-AC099850.3 + oe-NC group.

Sc scratch experiments and Transwell assays were performed to evaluate cell migration and invasion abilities. The results indicated (Fig. 4F, G) a significant decrease in the migration and invasion abilities of HepG2.2.15 cells in the si-AC099850.3 and si-CD276 group compared to the si-NC group. Conversely, the si-AC099850.3 + oe-CD276 group exhibited a significant enhancement in cell migration and invasion abilities compared to the si-AC099850.3 + oe-NC group. Furthermore, Western blot analysis demonstrated (Fig. 4H) a significant increase in E-cadherin protein levels and a significant decrease in CD276, N-cadherin, and Vimentin protein levels in HepG2.2.15 cells in the si-AC099850.3 and si-CD276 group compared to the si-NC group. Conversely, the si-AC099850.3 + oe-CD276 group showed a significant decrease in E-cadherin protein levels and a significant increase in CD276, N-cadherin, and Vimentin protein levels when compared to the si-AC099850.3 + oe-NC group.

In summary, AC099850.3 affects cell cycle progression and promotes the proliferation and invasion abilities of HepG2.2.15 cells by regulating the expression of immune checkpoint CD276.

Knocking down of AC099850.3 inhibits tumor growth in HBV-HCC bearing nude mice

To investigate the impact of AC099850.3/CD276 on HBV-HCC growth in nude mice, we established an HBV-HCC nude mouse model and injected si-NC, si-AC099850.3, si-AC099850.3 + oe-NC, or si-AC099850.3 + oe-CD276 HepG2.2.15 cells. After euthanizing the mice three weeks later, tumor tissue was removed and weighed. The results revealed (Fig. 5A) a significant reduction in tumor weight and volume in the si-AC099850.3 group compared to the si-NC group. Additionally, compared to the si-AC099850.3 + oe-NC group, the si-AC099850.3 + oe-CD276 group exhibited a significant increase in tumor weight and volume. qRT-PCR and Western blot analysis results (Fig. 5B, C) showed a significant decrease in AC099850.3 and CD276 mRNA and protein levels in tumor tissue of the si-AC099850.3 group compared to the si-NC group. Conversely, compared to the si-AC099850.3 + oe-NC group, the si-AC099850.3 + oe-CD276 group displayed a significant increase in CD276 mRNA and protein levels in tumor tissue. Furthermore, results from HE staining and TUNEL staining (Fig. 5D) demonstrated that tumor tissue cells in the si-AC099850.3 group exhibited necrosis and apoptosis compared to the si-NC group,

while the si-AC099850.3 + oe-CD276 group showed reduced levels of necrosis and apoptosis compared to the si-AC099850.3 + oe-NC group. Western blot analysis was used to evaluate the expression of proliferation-related proteins (Ki-67 and PCNA) (Fig. 5E), showing a decrease in Ki-67 and PCNA expression levels in tumor tissue of the si-AC099850.3 group compared to the si-NC group. On the other hand, the si-AC099850.3 + oe-CD276 group displayed an upregulation of Ki-67 and PCNA expression levels in tumor tissue compared to the si-AC099850.3 + oe-NC group.

In conclusion, the low expression of AC099850.3 inhibits tumor growth, leading to an increase in apoptotic cells in tumor tissue, while overexpression of CD276 can reverse the effect of low expression of AC099850.3 in nude mice.

Preparation, characterization, and drug release of CC@AC&SF@PP NPs nanocarriers

In this study, we discovered that AC099850.3 affects cell cycle progression by regulating the immune checkpoint CD276, promoting proliferation and invasion of HBV-HCC tumor cells. Hence, we prepared pH-triggered drug-eluting NPs called CC@AC&SF@PP NPs (Fig. 6A), which were designed to co-deliver AC099850.3 siRNA and SF to the HBV-HCC site for combination therapy. SF was encapsulated within pH-triggered positively-charged mPEG5K-PAE10K (PP) NPs using a single emulsion method, and AC099850.3 siRNA with negatively-charged was condensed on the surface of the drug-loaded NPs via electrostatic interactions. Finally, carboxymethyl chitosan (CMCS) was used to encapsulate the NPs. CMCS is negatively charged at physiological pH and positively charged in the tumor's acidic environment, allowing for targeted drug release.

To confirm the successful preparation of CC@AC&SF@PP NPs, we conducted comprehensive characterizations. TEM analysis showed that CC@AC&SF@PP NPs exhibited excellent dispersion and a uniform spherical appearance (Fig. 6B). Dynamic light scattering (DLS) measurements demonstrated a hydrodynamic diameter of CC@AC&SF@PP NPs as 130 ± 1.82 nm (Fig. 6C) and a zeta potential of -4.1 ± 0.13 mV (Fig. 6D). Additionally, by comparing the absorbance spectra of CC@AC&SF@PP NPs with SF@PP NPs, free AC099850.3 siRNA, and PP NPs, overlay features were observed in terms of peak height, peak area, and peak shape (Fig. 6E). This indicates that both SF and AC099850.3 siRNA were successfully loaded onto PP NPs, with the characteristic overlapping absorbance peak of CC@AC&SF@PP NPs appearing at 271 nm. Moreover, pH-dependent drug release profiles of CC@AC&SF@PP NPs were studied by dialysis and HPLC (Fig. 6F). The results showed that under acidic physiological conditions
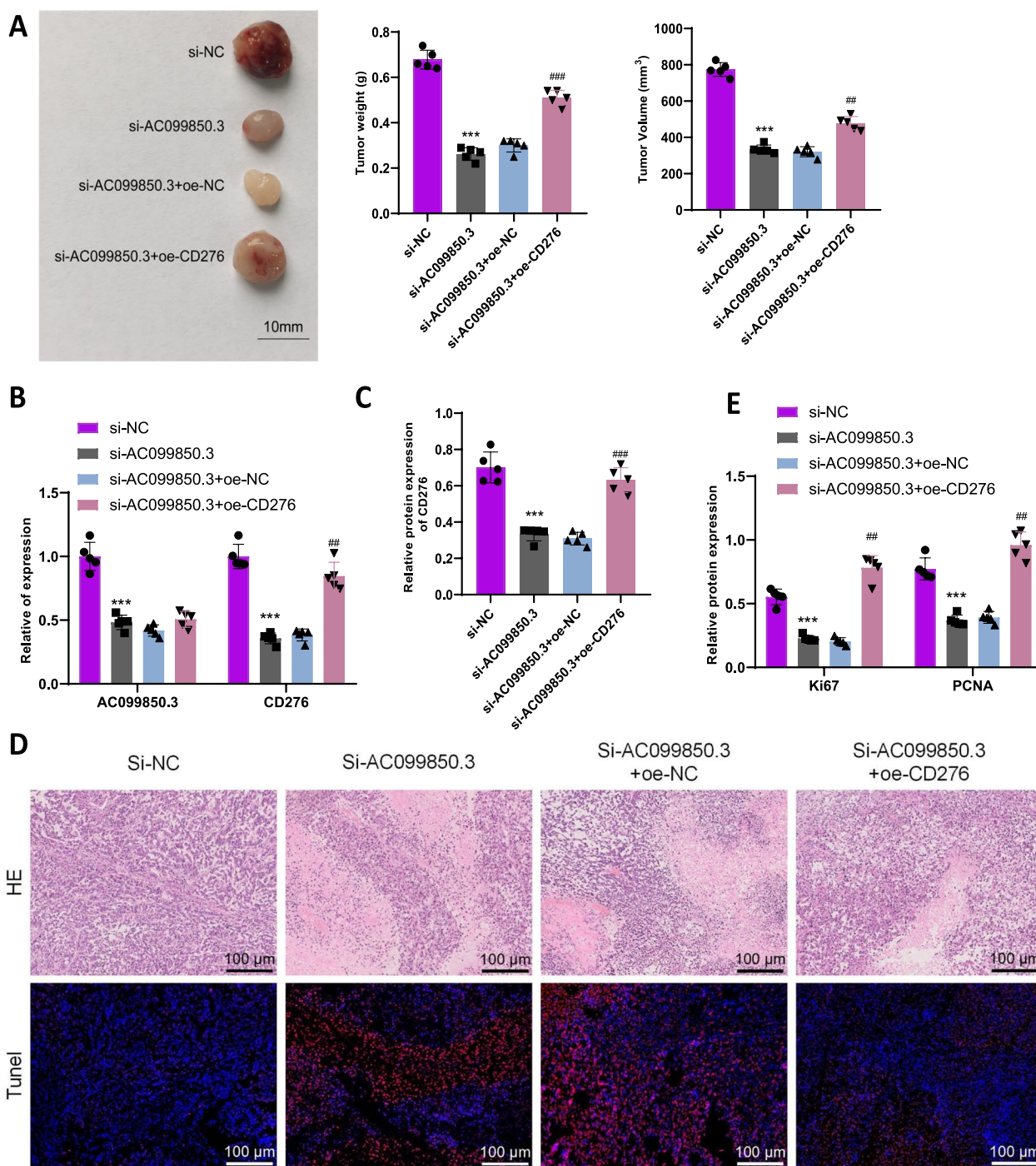
Fig. 5 Impact of AC099850.3/CD276 expression on HepG2.2.15 cells. **A** Tumor images, as well as statistics of tumor weight and volume in the subcutaneous tumors of each group of nude mice; **B**, **C** RT-qPCR and Western blot analysis assessing the expression levels of AC099850.3 and CD276; **D** HE staining to detect cell necrosis in tumor tissue, TUNEL staining to detect cell apoptosis in tumor tissue (Scale bar: 100 μm); **E** Western blot analysis measuring the expression levels of proliferation-related proteins (Ki-67 and PCNA) in tumor tissue; *** denotes comparison with the si-NC group, $P < 0.001$; ## denotes comparison with the si-AC099850.3 + oe-NC group, $P < 0.01$; ### denotes comparison with the si-AC099850.3 + oe-NC group, $P < 0.001$; N = 5
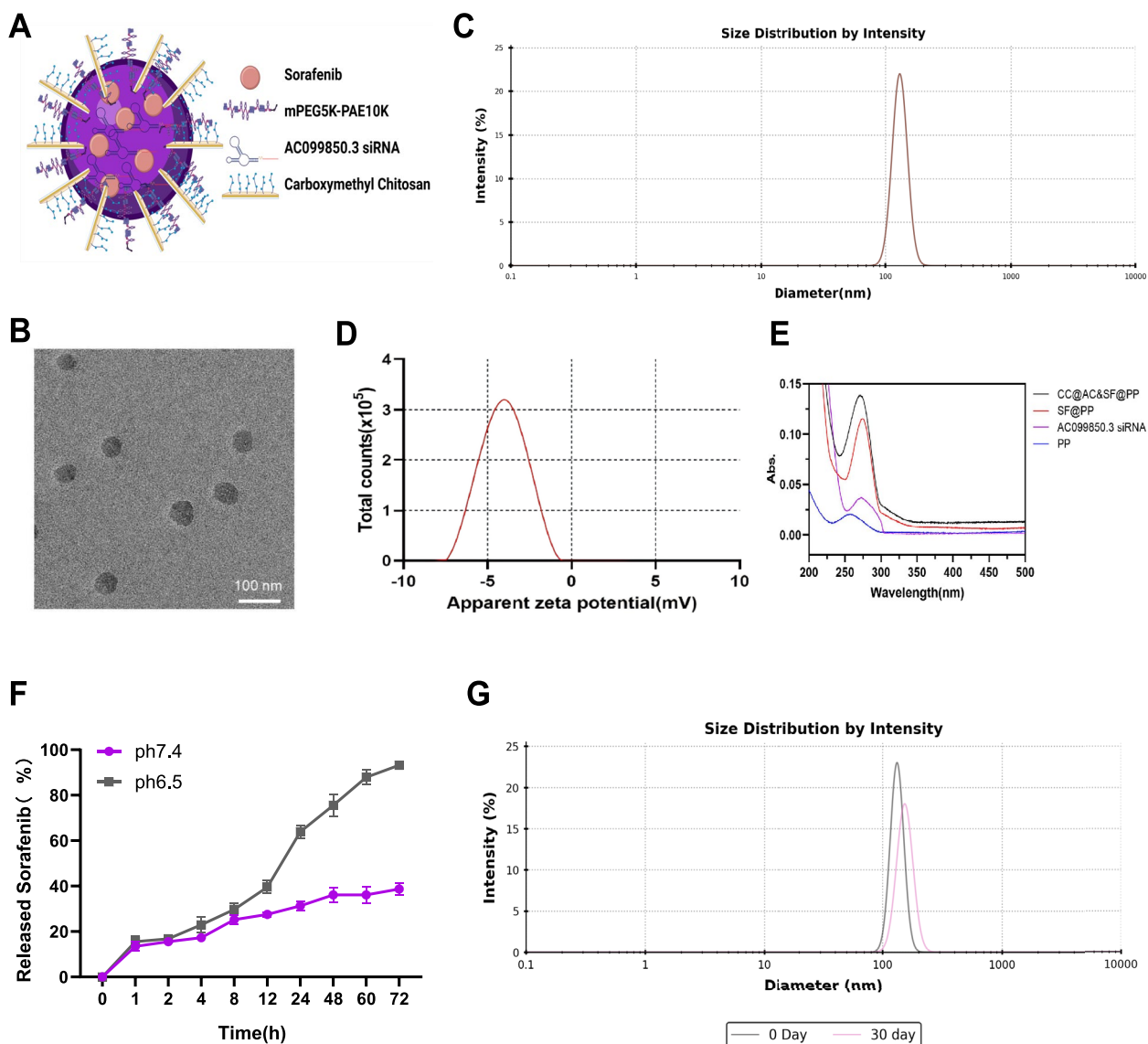
Fig. 6 Preparation, characterization, and drug release of CC@AC&SF@PP NPs. **A** Schematic representation of drug elution from the CC@AC&SF@PP NPs triggered by pH; **B** Representative TEM image of CC@AC&SF@PP (Scale bar: 100 nm); **C** Size distribution of CC@AC&SF@PP measured by DLS; **D** Zeta potential of CC@AC&SF@PP; **E** Ultraviolet–visible absorption spectra of PP NPs, AC099850.3 siRNA, SF@PP NPs, and CC@AC&SF@PP NPs; **F** In vitro SF release profile from CC@AC&SF@PP NPs in PBS buffer at pH 7.4 and 6.5; **G** Size of CC@AC&SF@PP on day 0 and day 30

(PBS, pH = 6.5), CC@AC&SF@PP NPs exhibited accelerated release rates with a sustained release rate even after 72 h, reaching a release rate of 88–94% for SF. Conversely, under normal physiological conditions (PBS, pH = 7.4), the release rate of CC@AC&SF@PP NPs was relatively low, ceasing after 48 h and achieving a maximum drug release rate of less than 40%. This demonstrates the ability of CC@AC&SF@PP NPs to sustain release in the acidic tumor tissue environment, making them a potential candidate for an ideal tumor microenvironment-triggered drug delivery system. Furthermore, stability analysis results (Fig. 6G)

revealed that CC@AC&SF@PP NPs maintained high colloidal stability after 30 days of storage in sterile water without DNA/RNA.

In conclusion, we successfully prepared CC@AC&SF@PP NP nanocarriers with excellent monodispersity, sustained release properties, and stability.

He *et al. Journal of Translational Medicine*   (2024) 22:809

Page 12 of 26

Downregulation of AC099850.3 and CD276 expression by CC@AC&SF@PP inhibited the proliferation and invasion abilities of HepG2 2.2.15 cells

In this study, we investigated the cellular uptake capacity of CC@AC&SF@PP NPs in HepG2 2.2.15 cells. HepG2 2.2.15 cells were exposed to a culture medium containing Cy3-AC099850.3 siRNA or CC@AC&SF@PP NPs and incubated for 6 h at pH 7.4 or 6.5. The results (Fig. 7A) showed strong fluorescence intensity in the groups treated with CC@AC&SF@PP NPs at pH 6.5, as well as the siRNA&Lipo2000 complex, whereas only weak fluorescence was observed in the Cy3-AC099850.3 siRNA group or the CC@AC&SF@PP NPs treated group at pH 7.4. This indicates that CC@AC&SF@PP NPs were effectively internalized by the cells. Furthermore, we investigated whether CC@AC&SF@PP NPs could reduce AC099850.3 expression and affect CD276 expression at the cellular level. The results of RT-qPCR and Western blot experiments (Fig. 7B, C) showed that compared to the Control group, there was no significant difference in the expression levels of AC099850.3 and CD276 in HepG2 2.2.15 cells treated with CC@PP, whereas a significant decrease in expression levels was observed in the CC@AC&SF@PP group and the siRNA&Lipo2000 group. Moreover, the expression levels of AC099850.3 and CD276 in the CC@AC&SF@PP group were lower than those in the siRNA&Lipo2000 group.

The results of the cell cycle analysis (Fig. 7D) showed no significant difference in the G2/M phase cell proportion of HepG2.2.15 cells between the Control group and the CC@PP group. However, a significant increase in the G2/M phase cell proportion was observed in the CC@AC&SF@PP group and the AC&SF group, indicating G2/M phase cell cycle arrest, with more pronounced arrest in the CC@AC&SF@PP group. The results of the CCK-8 assay and colony formation assay (Fig. 7E, F) demonstrated that the proliferation ability of HepG2.2.15 cells in the CC@PP group showed no significant difference compared to the Control group, whereas the proliferation ability of HepG2.2.15 cells was significantly compromised in the CC@AC&SF@PP group and the AC&SF group, with more significant reduction in the CC@AC&SF@PP group. Flow cytometry analysis (Fig. 7G) revealed enhanced apoptosis in HepG2.2.15 cells in the CC@AC&SF@PP group and the AC&SF group, with a more pronounced enhancement in the CC@AC&SF@PP group. Scratch and Transwell assays (Fig. 7H, I) demonstrated that compared to the Control group, there was no significant difference in the migration and invasion abilities of HepG2.2.15 cells in the CC@PP group, whereas a significant decrease was observed in the CC@AC&SF@PP group and the AC&SF group, with more significant reduction in the CC@AC&SF@PP group. Furthermore,

the results of Western blot analysis (Fig. 7J) showed no significant difference in the protein levels of E-cadherin, N-cadherin, and Vimentin in HepG2.2.15 cells between the Control group and the CC@PP group, whereas there was a significant increase in the E-cadherin protein level and a significant decrease in the N-cadherin and Vimentin protein levels in the CC@AC&SF@PP group and the AC&SF group.

These results indicate that CC@AC&SF@PP NPs can be effectively internalized by HepG2 2.2.15 cells, leading to the downregulation of AC099850.3 and CD276 expression, which in turn affects cell cycle progression and promotes proliferation and invasion abilities in HepG2 2.2.15 cells.

Enhancing the delivery of siRNA and SF in tumor tissue through CC@AC&SF@PP NPs

To further investigate the delivery efficacy of CC@ AC&SF@PP NPs loaded with Cy5-AC099850.3 siRNA and SF in tumor tissue, we performed an experiment as depicted in Figure S5A. Six hours after intraperitoneal injection, a noticeable fluorescence intensity was observed in the abdominal cavity, indicating the rapid clearance of free siRNA in vivo. In contrast, CC@ AC&SF@PP NPs containing the same concentration of Cy5-AC099850.3 siRNA exhibited bright fluorescence solely in the liver, with even more prominent fluorescence observed at the tumor site within the liver. This indicates the stability of the NPs in vivo and their successful enhancement of siRNA delivery to the tumor region. Subsequently, we conducted ex vivo imaging of various tissues and organs in mice (Figure S5B), which further confirmed the high accumulation of NPs in the liver tumor tissue, while free siRNA was rapidly metabolized through the liver and kidneys. To demonstrate the accurate cellular delivery and release of CC@AC&SF@PP NPs in the tumor region, tumor tissue slices were obtained at the white dashed line in Figure S5B. As shown in Figure S5C, the tumor region treated with CC@AC&SF@ PP NPs exhibited an enhanced Cy5 fluorescence signal, primarily distributed around the hepatic lobes, corresponding to the location of tumor growth in Figure S5B. This indicates that CC@AC&SF@PP NPs exhibit targeting and specificity, accurately releasing the drug in the slightly acidic microenvironment of tumor tissue. Conversely, due to its nonspecific nature, free siRNA displayed a uniform fluorescence distribution in the tumor slices. Additionally, in the toxicity assessment experiment of the NPs (Figure S5D), no tissue damage, necrosis, or inflammation were observed in the slices treated with CC@AC&SF@PP NPs, both in the short-term (1 day) and long-term (7 days), providing ample evidence for
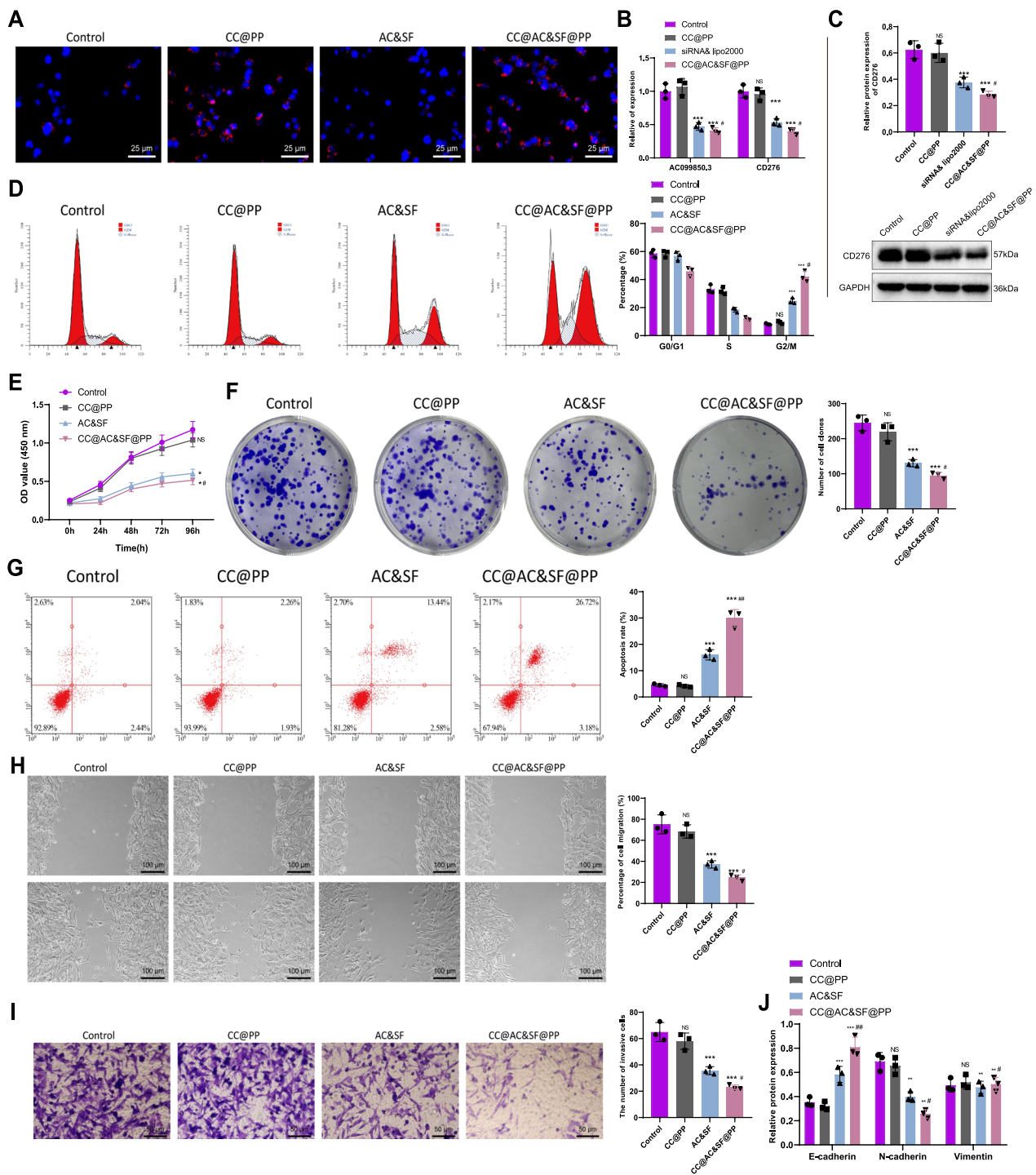
Fig. 7 Effect of CC@AC&SF@PP NPs on HepG2.2.15 cells. **A** The cellular uptake capacity of CC@AC&SF@PP NPs in HepG2 2.2.15 cells at pH 6.5 and 7.4. The strong fluorescence intensity observed at pH 6.5 indicates effective internalization by the cells; **B**, **C** Expression levels of AC099850.3 and CD276 measured by RT-qPCR and Western blot; **D** Flow cytometry analysis of cell cycle and statistical histograms showing cell cycle phase distribution; **E**, **F** Cell proliferation measured by CCK-8 assay and colony formation experiment; **G** Apoptosis assay by flow cytometry; **H**, **I** Cell migration and invasion abilities evaluated by scratch assay (Scale bar: 100 μm) and Transwell assay (Scale bar: 50 μm); **J** Expression levels of E-cadherin, N-cadherin, and Vimentin in HepG2.2.15 cells determined by Western blot; NS represents no significant difference compared to the Control group; ** represents significant difference compared to the Control group, P < 0.01; *** represents significant difference compared to the Control group, P < 0.001; # represents significant difference compared to the AC&SF group, P < 0.05; ## represents significant difference compared to the AC&SF group, P < 0.01; all cellular experiments were repeated three times

He *et al. Journal of Translational Medicine*   (2024) 22:809

Page 14 of 26

the excellent biocompatibility of CC@AC&SF@PP NPs in vivo.

Finally, we evaluated the in vivo anti-tumor efficacy of CC@AC&SF@PP NPs in a mouse HBV-HCC in situ tumor model. Mice were divided into PBS, CC@PP, CC@AC@PP, CC@NC&SF@PP, CC@AC&SF@PP, and AC&SF groups, administered via tail vein injection once every three days, and tumor growth was observed. The tumor size was measured by a small animal imaging system based on the intensity of bioluminescence (Fig. 8A). Compared to the PBS group, the CC@PP group did not exhibit any inhibitory effect on tumor growth. The CC@AC@PP and CC@NC&SF@PP groups showed suboptimal inhibition of tumor growth. The AC&SF group, using a combination therapy based on free diffusion, was able to partially suppress tumor growth. However, the CC@AC&SF@PP group demonstrated a more pronounced inhibition of tumor growth. In comparison to the CC@PP group, the CC@NC&SF@PP group exhibited a moderate inhibitory effect on tumor growth. These results indicate that the synergistic enhancement of treatment effects between AC099850.3 siRNA gene therapy and SF in vivo leads to significant inhibition of tumor growth. Subsequently, tumor growth curves were obtained by measuring the bioluminescence intensity of tumor tissue (Fig. 8B). On the 16th day after the first injection, mice were sacrificed, and the entire liver was collected. These results were consistent with the imaging system observations, with the lowest level of tumor growth observed in mice treated with CC@AC&SF@PP NPs (Fig. 8C). Results from the RT-qPCR and Western blot experiments (Fig. 8D, E) indicated that the free siRNA exhibited instability and non-specific absorption in vivo, along with rapid clearance in the liver and kidneys. AC&SF only partially inhibited the expression of AC099850.3 and CD276 in vivo, whereas CC@AC&SF@PP NPs and CC@AC@PP NPs benefited from the protective effect of the CMCS shell and the pH-triggered delivery system, promoting the delivery of AC099850.3 siRNA to tumor tissue and enhancing its transfer to tumor cells, thus reducing the expression of AC099850.3 and CD276 in the tumor tissue. Additionally, immunohistochemical results (Fig. 8F)

demonstrated a significant decrease in CD276 expression levels in the AC&SF, CC@AC&SF@PP, and CC@AC@PP groups compared to the PBS and CC@PP groups, with CC@AC&SF@PP and CC@AC@PP groups showing a more significant decrease. Results from HE staining and TUNEL staining (Fig. 8G) revealed necrosis and apoptosis of tumor tissue cells in the PBS and CC@PP groups, partial alleviation of necrosis and apoptosis in the AC&SF and CC@AC@PP groups, and a significant alleviation of necrosis and apoptosis in the CC@AC&SF@PP group.

These findings suggest that the pH-sensitive CC@AC&SF@PP can be an ideal platform in the acidic tumor environment for enhancing the delivery of siRNA and SF to tumor cells, thereby enhancing the tumor suppression effect.

Discussion

HBV-HCC is one of the most common types of liver cancer worldwide, and its treatment faces numerous challenges [1, 40]. The mechanism of HBV-HCC development is complex, involving viral evasion mechanisms, immune tolerance, and the influence of the tumor microenvironment [40, 41]. Currently, conventional treatment methods include chemotherapy and tumor resection, but drug resistance and high recurrence rates are often encountered [42, 43]. In recent years, immunotherapy has emerged as a promising new treatment strategy for HBV-HCC [44–46]. Current research primarily focuses on exploring new therapeutic targets and developing innovative treatment strategies to improve the efficacy of HBV-HCC treatment [47, 48].

In this study, it was found that the expression of AC099850.3 and the immune checkpoint CD276 is associated with tumor growth and progression in HBV-HCC [19]. This is consistent with similar results observed in previous studies in other types of tumors [4, 36]. The immune checkpoint CD276 plays a key role in suppressing the immune response and promoting tumor escape [19]. The findings of this study further deepen our understanding of the functions and regulatory mechanisms of AC099850.3 and CD276 in HBV-HCC.

(See figure on next page.)

Fig. 8 Effects of CC@AC&SF@PP NPs on HepG2.2.15 cells. **A** Real-time visualization of tumors in mice from different groups. Bioluminescent images were obtained by injecting 150 μL of a 15 mg/mL solution of d-luciferin potassium salt into the peritoneal cavity on days 2, 5, 8, 11, and 14 after drug administration (day 1 post-injection); **B** Tumor volume growth curves of mice after different treatments. Tumor size was measured by bioluminescent intensity using the Xenogen IVIS SPECTRUM small animal imaging system; **C** Representative photographs of mouse livers on day 16; **D**, **E** Expression levels of AC099850.3 and CD276 measured by RT-qPCR and Western blot; **F** Immunohistochemical staining and quantitative analysis of CD276 in tumor tissues from different groups (Scale bar: 25 μm); **G** Evaluation of tumor cell necrosis by H&E staining and apoptosis by TUNEL staining in tumor tissues (Scale bar: 100 μm); * represents significant difference compared to the PBS group, $P < 0.05$; ** represents significant difference compared to the PBS group, $P < 0.01$; *** represents significant difference compared to the PBS group, $P < 0.001$; ## Compared to the CC@PP group, $P < 0.01$; N = 5
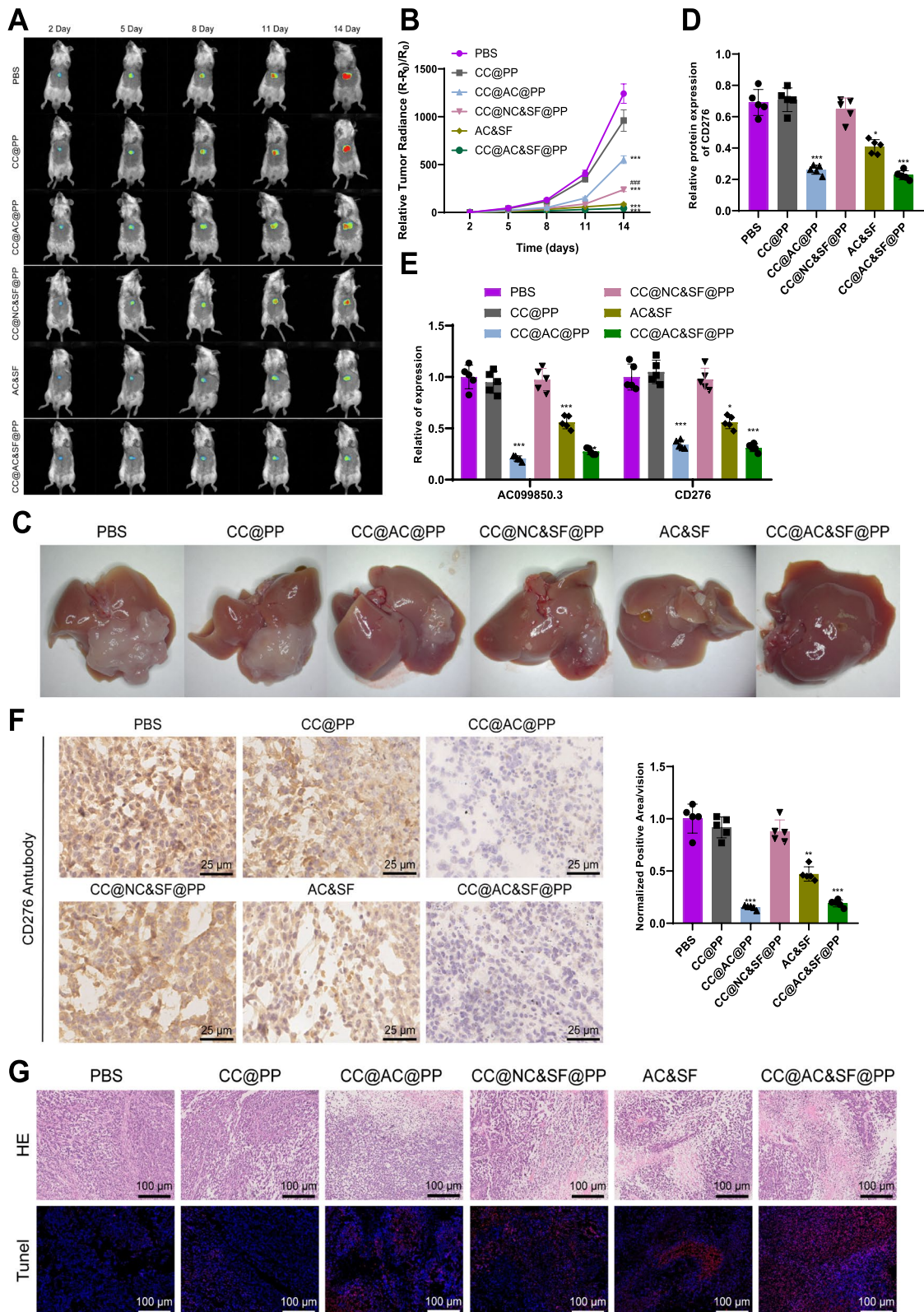
Fig. 8 (See legend on previous page.)

AC099850.3 may regulate CD276 through several molecular mechanisms. Primarily, it could enhance CD276 transcription by interacting with specific transcription factors or chromatin modifying factors. Additionally, AC099850.3 might stabilize CD276 mRNA, prolonging its half-life to ensure sustained expression. Furthermore, it could influence signaling pathways such as PI3K/AKT or MAPK/ERK, known to be associated with cell proliferation and immune checkpoint regulation. These pathways could further impact the expression and functional activity of CD276.

This study reveals the mechanism by which AC099850.3 regulates the expression of the immune checkpoint CD276 in HBV-HCC, and this regulation affects tumor proliferation and invasion by influencing the progression of the cell cycle (Fig. 9). This is in line with the functions of AC099850.3 observed in previous studies in different types of tumors [49, 50]. The regulation of the cell cycle plays a crucial role in tumor development [51]. Therefore, this study is of significant importance for understanding the specific mechanisms of AC099850.3 in the progression of HBV-HCC.

The regulation of CD276 by AC099850.3 potentially involves multiple pathways. Studies indicate that AC099850.3 can interact with key signaling molecules like STAT3, which is known for its role in immune checkpoint regulation. By modulating STAT3 activity, AC099850.3 may indirectly impact CD276 expression.

Moreover, AC099850.3 could alter the epigenetic landscape of the CD276 promoter region, modifying chromatin accessibility to facilitate transcriptional activation. These interactions underscore the complexity of the regulatory network between AC099850.3 and CD276.

This study successfully prepared a novel nanoparticle carrier, CC@AC&SF@PP, and applied it to the combination therapy of HBV-HCC. The nanoparticle carrier successfully delivered AC099850.3 siRNA and SF to the HBV-HCC site and showed the potential to enhance the efficacy of combination therapy. The design of this nanoparticle enables precise drug delivery and sustained release, thereby increasing the local drug concentration and duration of action, improving the therapeutic efficacy, and reducing side effects [52].

Based on the results, we can preliminarily draw the following conclusions: AC099850.3 accelerates the cell cycle progression and promotes the occurrence and development of HBV-HCC by upregulating the expression of immune checkpoint CD276. CC@AC&SF@PP NPs are loaded with AC099850.3 siRNA and SF for the purpose of combined therapy in situ HBV-HCC.

Future research should focus on identifying the precise molecular interactions between AC099850.3 and CD276. Techniques such as immunoprecipitation and chromatin immunoprecipitation experiments can be employed to determine the binding partners of AC099850.3 and their impact on the CD276 promoter region. Furthermore,
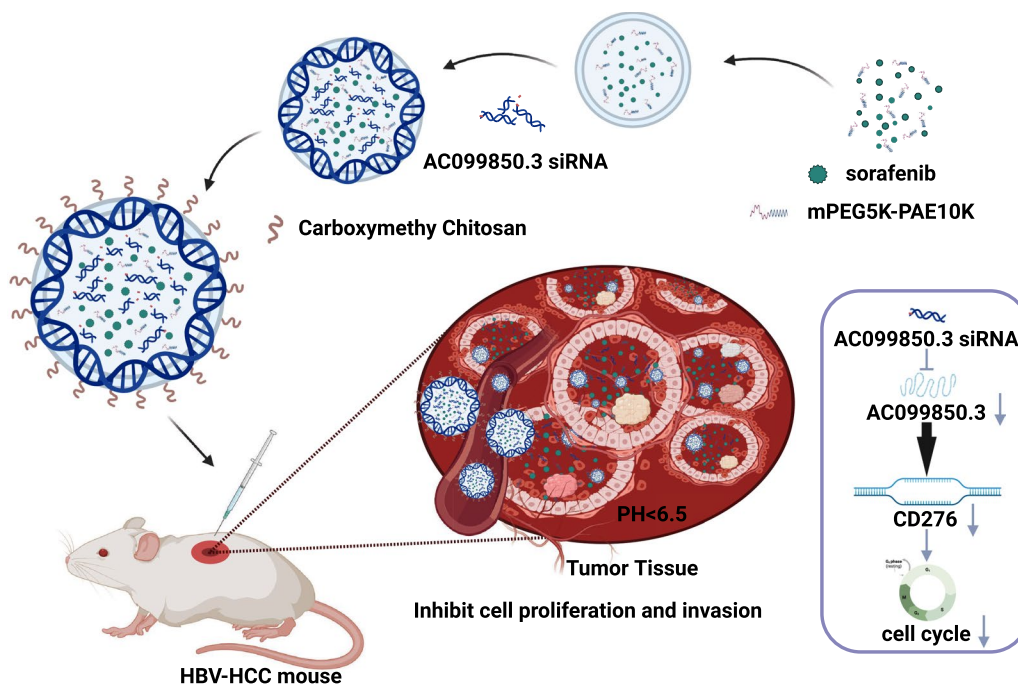

Fig. 9 AC099850.3 regulates immune checkpoint CD276 to modulate HBV-HCC cell proliferation and invasion: a novel strategy for SF and immune checkpoint combination therapy

He *et al. Journal of Translational Medicine*   (2024) 22:809

Page 17 of 26

investigating the downstream signaling pathways activated by CD276 under high levels of AC099850.3 can provide deeper insights into the proliferation and invasion mechanisms in HBV-HCC cells. Understanding these pathways is crucial for developing targeted therapies to disrupt the AC099850.3-CD276 axis.

This study carries significant scientific and clinical value. Firstly, we constructed a prognostic risk model with good sensitivity and specificity, which can be used to predict the survival of HBV-HCC patients through screening and analysis of the TCGA database and survival information. Secondly, through differential analysis and validation experiments, we identified AC099850.3 as a key gene and discovered its promotion of cell cycle progression in HBV-HCC by regulating immune checkpoint CD276 expression. Furthermore, we successfully prepared NPs loaded with AC099850.3 siRNA and SF, demonstrating their potential advantages in treating in situ HBV-HCC.

Despite the important findings of this study, there are still limitations. Firstly, the results of this study need further validation and confirmation due to the limited sample size. Secondly, the research results in animal models may differ from the actual situation in human patients. Therefore, more preclinical studies are needed to verify the effectiveness and safety of AC099850.3 and CC@ AC&SF@PP NPs in HBV-HCC treatment further.

In future perspectives, further research can be conducted in several aspects. Firstly, larger sample sizes and multicenter clinical studies can be combined to verify the effectiveness and clinical application value of the prognostic risk model in different populations. Secondly, the role of AC099850.3 in HBV-HCC can be further studied to explore its interaction with other immune checkpoints and its potential in immune therapy. Lastly, clinical trials can be carried out to further validate the therapeutic efficacy and safety of nanoparticle drug delivery systems in HBV-HCC patients, promoting the clinical translation of this technology.

Methods

Retrieval of transcriptome sequencing data

We obtained gene expression data and survival information for liver cancer patients from the UCSC Xena database (https://xena.ucsc.edu/). The downloaded data was in FPKM format. Additionally, we retrieved clinical data for liver cancer patients from the TCGA database, including HBV information, as described in [53]. From this data, we extracted the clinical data for HBV-HCC patients (Table S6). Since these data were sourced from publicly available databases, no ethical approval or informed consent was required.

Construction of weighted gene co-expression networks

We performed clustering analysis on the HBV-HCC samples using the "hclust" package in R software to establish a co-expression network. Subsequently, the "WGCNA" package in R was utilized to construct the gene co-expression network. To build the weighted co-expression network, we selected the top 25% of genes ranked by variance and calculated the Pearson correlation coefficients between them. We determined an appropriate soft thresholding power β to meet the criteria for a scale-free network. The adjacency matrix was transformed into a topological overlap matrix (TOM), and hierarchical clustering was applied in the gene-level hierarchical clustering tree. The MEbrown module, which showed the highest correlation with survival status, was selected for further analysis. Next, we downloaded immune-related gene sets from the ImmPort database and extracted immune-related mRNA from the MEbrown module. Finally, we identified lncRNA with correlation to the immune-related mRNA in the MEbrown module [54].

Extraction of mRNA and lncRNA related to immunity

To extract genes related to immunity, we utilized the ImmPort database (https://www.immport.org/shared/home). The "UpSetR" package in R software was employed to intersect the MEbrown module genes from the co-expression network weighted by gene expression and the gene set associated with immunity. This intersection provided us with a collection of mRNA genes related to immunity. We then employed a matrix correlation analysis tool to examine the correlation between mRNA and lncRNA. By setting the threshold at R=0.4 and P < 0.001, we obtained lncRNA data that were associated with immunity [55, 56].

Construction of prognostic risk model and prognostic correlation analysis

In this study, we divided a total of 44 HBV-HCC patient samples from the TCGA database into a training set (Train, including 24 patient samples) and a testing set (Test, including 20 patient samples) using a random method. We utilized the "survival" package in the R language to perform univariate Cox regression analysis on genes related to overall survival, selecting genes with a significance level of P < 0.05 and hazard ratios (HR) as potential candidate biomarkers. Subsequently, we employed the LASSO Cox regression model to determine the optimal coefficients and calculate the penalized likelihood. Based on the highest lambda value (lambda. min) obtained from 1000-fold cross-validation in the LASSO method, we identified a set of prognostic genes along with their corresponding LASSO coefficients and

He *et al. Journal of Translational Medicine*   (2024) 22:809

Page 18 of 26

ultimately constructed a prognostic risk model based on the expression levels of these genes. The calculation method for the prognostic model score is as follows: Prognostic score $= (\beta1 \times$ expression level of gene $1) + (\beta2 \times$ expression level of gene $2) + \ldots + (\beta n \times$ expression level of gene n).

Using the median score of the training set as the cutoff, we divided the training set, testing set, and the entire sample set (All) into high-risk and low-risk groups. We evaluated whether the risk score could serve as an independent prognostic factor through univariate Cox analysis and multivariate Cox analysis. Additionally, we compared the overall survival difference between the high-risk and low-risk groups using Kaplan–Meier survival curves, using a significance level of $P < 0.05$. The "timeROC" package in R was employed to plot the ROC (receiver operating characteristic) curve of the prognostic risk model, and the accuracy of the prognostic risk model for HBV-HCC patient prognosis was assessed based on the area under the curve (AUC). Lastly, using the "survival" package and "survminer" package in R, we plotted the survival curves of the prognostic risk model and calculated the corresponding P-values [57–59].

Differential gene analysis

We performed differential gene analysis using HBV-HCC RNA-Seq data, consisting of 50 normal samples and 44 tumor samples. To identify differentially expressed genes, we applied filter conditions of |log2FC| > 1 and $P < 0.05$, using the limma package in R. Subsequently, we generated a heatmap and a volcano plot using the pheatmap and ggplot2 packages in R, respectively. Additionally, we employed the ggplot2 package to visualize gene expression patterns among the 50 normal and 44 tumor samples. Furthermore, we extracted 8 pairs of matched samples and illustrated the gene expression profiles of key genes in these paired samples. All analyses were performed using R version 4.2.1 (R Foundation for Statistical Computing) [56].

Bioinformatics analysis of key genes in HBV-HCC

Based on the median expression values of key genes, we divided the HBV-HCC tumor samples into high and low-expression groups. The overall survival difference between the high and low expression groups was compared using Kaplan–Meier survival curve analysis, with a cutoff value of $P < 0.05$. We utilized the "timeROC" package in R language to draw time-related ROC curves and assess the accuracy of disease status prediction based on gene expression.

CIBERSORT is a gene expression-based deconvolution algorithm used to describe the cellular composition of complex tissues. We stratified the samples into high and low-expression groups based on the expression levels of key genes. By combining the "e1071" and "preprocessor" packages in R software with the CIBERSORT algorithm, immune cell composition analysis was performed on HBV-HCC tumor samples. The content of immune cells was calculated for each sample and simulated 100 times, with results with $P < 0.05$ retained. Subsequently, the "vioplot" package in R software was used for differential analysis of immune cells. The correlation between immune cells was evaluated using the "ggplot2," "ggpubr," and "ggExtra" packages in R software, employing Spearman's correlation coefficient. To investigate the relationship between AC099850.3 and immune checkpoint as well as AC099850.3 and tumor mutation burden, the "ggplot2" and "ggpubr" packages in R software were employed, and results with $P < 0.05$ were retained [60–65].

Gene function enrichment analysis

A tool for calculating matrix correlation was used to analyze the correlation between AC099850.3 and the gene expression matrix. Based on the threshold of $R = 0.7$ and $P < 0.001$, the co-expressed genes of AC099850.3 were identified. The "clusterProfiler" package in R was utilized for Gene Ontology (GO) and KEGG enrichment analysis of AC099850.3 and its co-expressed genes. Subsequently, the "enrichplot" package was employed to generate bar plots and bubble plots for the enrichment results of three GO categories: biological process (BP), cellular component (CC), and molecular function (MF). Furthermore, bar plots and bubble plots were produced for the KEGG enrichment analysis results [66].

In vitro cell culture

HepG2 2.2.15 (CL0549) human liver cancer cells infected with HBV were purchased from Fenghui Biotech. The cells were cultured in a specific medium for HepG2/2.2.15 (CM-0594, Procell), which comprised MEM (containing NEAA) + 10% FBS + 380 µg/mL G418 + 1% P/S [67].

Cell treatment and grouping

When HepG2 2.2.15 cells were in the logarithmic growth phase, they were digested with trypsin and seeded at a density of 1×10^5 cells per well in a 6-well plate. After conventional incubation for 24 h, when the cell confluency reached approximately 75%, cell transfection was performed according to the transfection protocol of Lipofectamine 2000 (11668-019, ThermoFisher). The plasmid concentration used was 50 ng/mL. The target sequences for siRNA were as follows: AC099850.3-siRNA1: CTGCTATGGACTTCAGAGA; AC099850.3-siRNA2: CCAGGCTGTATTACTGTCT; AC099850.3-siRNA3: GCG

He *et al. Journal of Translational Medicine*   (2024) 22:809

Page 19 of 26

TCACCATGCCTGGGTA; CD276-siRNA1: CAACGA GCAGGGCTTGTTTGA; CD276-siRNA2: CTAGCC TTAATACTGGCCTTT; CD276-siRNA3: GCTTGT TTGATGTGCACAGCA. The overexpression vector pcDNA3.1 and siRNA sequences were designed and constructed by Gima Genes (Shanghai, China), and the knockout efficiency was validated using RT-qPCR.

HepG2 2.2.15 cells are seeded at a density of 5×10^5 cells per well in a 6-well plate and incubated for 24 h in a fresh culture medium. After centrifugation to remove the culture medium, the cells are washed with PBS and resuspended in 1 mL of opti-MEM (31985070, ThermoFisher) medium. Then, 5 μL of CC@PP, CC@AC&SF@PP, and AC&SF (siRNA concentration of 20 μM, pH 6.5) are added, respectively. After 6 h, 1.5 mL of fresh culture medium is added. Cells are collected for subsequent analysis after 72 h.

The cells were divided into the following groups for the study: si-NC group (transfected with lentivirus si-NC), si-AC099850.3 group (transfected with lentivirus AC099850.3-siRNA2), si-CD276 group (transfected with lentivirus CD276-siRNA2), si-AC099850.3 + oe-NC group (co-transfected with lentivirus AC099850.3-siRNA2 and oe-NC transfected with empty vector), si-AC099850.3 + oe-CD276 group (co-transfected with lentivirus AC099850.3-siRNA2 and oe-CD276, where oe-CD276 denotes cells overexpressing the CD276 gene), Control group, CC@PP group (treated with CMCS-coated mPEG5K-PAE10K NPs), CC@AC&SF@PP group (treated with a combination of AC099850.3 siRNA and SF co-loaded mPEG5K-PAE10K NPs), and AC&SF group (treated with free AC099850.3 siRNA and SF) [68].

Cell cycle analysis

HepG2 2.2.15 cells were collected and washed twice with PBS buffer. Subsequently, the cells were suspended in pre-chilled PBS containing 70% ethanol and incubated at 4 ℃ for 4 h. Afterward, the cells were washed twice with pre-chilled PBS and incubated with PBS containing 0.2% Triton X-100 and 10 μg/mL RNase at 37 ℃ for 30 min. Following the incubation, the cells were stained with 400 μL propidium iodide (PI) solution (50 g/mL, HY-D0815, MCE) in the dark at 4 ℃ for 30 min. Finally, the cell cycle distribution was analyzed using a flow cytometer (Cyto-FLEX, Beckmancoulter) and the accompanying software [69].

CCK-8 assay

Transfected HepG2.2.15 cells (100 μL) were seeded into a 96-well plate and incubated in a cell culture incubator for 0, 24, 48, 72, and 96 h. After the respective incubation periods, CCK-8 reagent (K1018, Apexbio) was added to each well, followed by a 2-h incubation period. The absorbance was measured at 450 nm [67]. Each experiment was performed with 5 parallel wells and repeated independently three times.

Clone formation assay

After cell transfection, the cells were seeded at a density of 1×10^5 cells per well in a 6-well plate and incubated for 2–3 weeks until visible cell clones were formed. The culture medium was then aspirated, and the cells were washed with PBS. Next, 4% paraformaldehyde was added to each well for cell fixation, and the cells were incubated for 15 min. After removing the fixative, 1 mL of Giemsa staining solution (C0131, Beyotime) was slowly added along the walls of each well, and the cells were stained in the dark for 20 min. Subsequently, the Giemsa staining solution was washed away with running water. The 6-well plate was inverted onto a clean paper towel, and the number of cell clones was calculated [67].

Transwell assay

Forty-eight hours after cell transfection, a Transwell invasion assay was performed. First, 50 μL of matrix gel (354234, BD Biosciences, USA) was coated in the Transwell chambers and allowed to solidify at 37 ℃ for 30 min. After coating, the chambers were rinsed with an FBS-free medium. Cells were diluted to a concentration of 2.5×10^4 cells/mL, and 100 μL of cell suspension was added to each well of the upper chamber, while 500 μL of medium supplemented with 10% FBS was added to the lower chamber. After 24 h, the chambers were removed, and the cells in the upper chamber were gently removed using a cotton swab. The cells were fixed with 4% PFA for 30 min at room temperature. Subsequently, the cells were stained with 0.1% crystal violet for 30 min. Five random areas were selected, and images were captured using an inverted microscope. The number of cells was then calculated [70, 71].

Scratch experiment

Logarithmic phase cells were harvested and prepared as a single-cell suspension at a concentration of 5×10^5 cells/mL. The cells were then evenly seeded in a 6-well plate. After 24 h, the cells in each group were subjected to the corresponding treatments and incubated in a 37℃, 5% CO_2 cell culture incubator for 24 h. A scratch was made on the surface of the cells in each well using a 100 μL sterile pipette tip. During scratching, the tip was kept vertical, and efforts were made to ensure that the width of scratches in each group was consistent. The culture medium in the 6-well plate was discarded, and the cells were washed twice with PBS. Serum-free medium was added for further incubation. The cells were observed and photographed, and the width of the scratch was

He *et al. Journal of Translational Medicine*   (2024) 22:809

Page 20 of 26

measured at 0 h as a control. The 6-well plate was placed in a 37℃, 5% CO_2 cell culture incubator for 24 h to allow cell migration. The migrated cells were observed and photographed, and the migration rate was calculated as (width of scratch at 0 h—width of scratch at 24 h) / width of scratch at 0 h × 100% [67].

Flow cytometry
The Annexin V-FITC Apoptosis Staining/Detection Kit (ab14085, abcam) was used for cell analysis. The cell density was adjusted to 1×10^5 cells/mL for each group. Three milliliters of cell suspension were taken for each group and centrifuged at 500 rpm for 5 min in a 10 mL centrifuge tube. After removal of the culture medium, the cells were resuspended in 100 μL of binding buffer, followed by the addition of 5 μL Annexin V-FITC and 5 μL PI. The mixture was gently mixed and incubated at room temperature in the dark for 15 min. Flow cytometry was performed to detect FITC fluorescence and PI fluorescence. Q1: Upper left quadrant (UL) represented cell debris with no cell membrane or dead cells due to other causes; Q2: Upper right quadrant (UR) represented late apoptotic cells; Q3: Lower left quadrant (LL) represented viable (live) cells; Q4: Lower right quadrant (LR) represented early apoptotic cells. The apoptotic rate was analyzed by assessing the percentages of cells in the Q2 and Q4 quadrants [67].

Subcutaneous transplanted tumor experiment in mice
All animal experiments in this study were conducted in accordance with the regulations and guidelines of our institutional animal ethics committee and approved by the committee. We made efforts to minimize animal pain and distress and to reduce the number of animals required for the experiments. Animal housing, handling, and experimental procedures were strictly performed according to internationally recognized animal welfare standards. Appropriate care was provided to all animals, and proper handling after the experiments was ensured. Male C57BL/6N nude mice (4–5 weeks old, weighing 18–22 g) were purchased from Beijing Vital River Laboratories. They were housed in SPF-grade animal facilities with constant humidity (45–50%) and temperature (25–27 °C) for 1 week, with a 12-h light–dark cycle, to acclimatize to the experimental environment. The mice fasted for 12 h prior to drug administration and were allowed free access to food and water at other times [72, 73]. All our animal experimental procedures were approved by our institutional animal ethics committee. We randomly divided 20 nude mice into 4 groups: si-NC group, si-AC099850.3 group, si-AC099850.3 + oe-NC group, and si-AC099850.3 + oe-CD276 group, with 5 mice in each group. HepG2.2.15 cells (5×10^6/0.2 mL)

were injected subcutaneously into the back of the mice. After 3 weeks, we measured the width (W) and length (L) of the tumors in each group using a caliper to monitor tumor growth and calculated tumor volume (V) using the formula $V = (W^2 \times L)/2$. The mice were euthanized, and the tumor tissues were dissected and removed for weighing. The tumor tissues were divided into two parts, with one part used for TUNEL staining and H&E staining and the other part frozen and stored in liquid nitrogen for subsequent experimental analysis [74, 75].

Hematoxylin and Eosin (H&E) staining
The tumor tissue was fixed in a 4% formalin solution at 4 °C for 8 h. Subsequently, it was soaked in a 70% ethanol solution for 5 min, followed by dehydration in a gradient of 80%, 90%, 95%, and absolute ethanol for 4 h. Then, the tissue was immersed in xylene for 30 min, embedded in paraffin, and cut into consecutive 3 μm-thick sections. A total of ten sections were taken from each sample for H&E staining. The sections were initially stained with hematoxylin (Sigma, H9627) for 5 min, followed by 5-min staining with 1% aqueous eosin (National Pharmaceutical Group, 71014544). Finally, the sections were soaked in water. After subsequent immersion in ethanol (National Pharmaceutical Group, 10009218) and xylene (National Pharmaceutical Group, 10023418), they were sealed with neutral gum (National Pharmaceutical Group, 10004160) and observed under an Olympus microscope (BX53) [69].

TUNEL assay
The tissue sections were incubated at room temperature for 20 min in a solution of 100 μL proteinase K (20 g/mL concentration) per section, ensuring complete coverage. After rinsing with deionized water, the sections were stained with a Cell Apoptosis Detection Kit (Solarbio, T2190) and DAPI (Beyotime, C1002). The stained sections were observed and photographed using an Olympus microscope (BX53) [69].

Preparation of SF@PP NPs
Analytical-grade chloroform, methanol, polyoxymethylene, triethylamine (TEA), and acetonitrile (ACN, HPLC) were obtained from the National Pharmaceutical Group. The biological materials and preparations used in this study were SF (HY-10201, 99.92%, MCE), mPEG5K-PAE10K (Q-0265422, Xi'an Qi Yue Biotechnology Co., Ltd.), carboxymethyl chitosan (CMCS, C9400, MW = 20,000–50,000, degree of carboxylation 87–90%, Solarbio), D-Luciferin potassium salt (HY-12591B, MCE), and DEPC water (HY-156262, MCE).

SF@PP NPs loaded with SF were prepared using a single emulsion method. 1 mg of SF was dissolved in 1 mL of chloroform/methanol (1:1, v/v) and dropped into a

He *et al. Journal of Translational Medicine*   (2024) 22:809

Page 21 of 26

stirring solution containing 10 mg of mPEG5K-PAE10K in 10 mL of chloroform/methanol (1:1, v/v). Then, the mixture was gently stirred for 1 h at room temperature before being dropped into 10 mL of pre-stirred DEPC water. The mixture was subjected to ultrasonication using an intelligent ultrasonic cell disruptor (SCIENTZ-950E, Ningbo Xinzhi Biotechnology Co., Ltd.) set at 275 W for 4 min, with the pulse off for 1.5 s after every 8 s to prevent excessive heat generation. After evaporating the organic solvent using a rotary evaporator, excess SF was removed by centrifugation at 4000 rpm for 20 min using an Amicon Ultra-15 centrifugal filter unit (UFC900324, Sigma). The filtrate was collected, and the residual amount of SF was determined by high-performance liquid chromatography. Finally, the synthesized SF@PP NPs solution was filtered through a syringe filter (0.45 μm, Millipore) and stored in DEPC water at 4 °C [28].

Preparation of AC&SF@PP NPs
A total of 5 μL of AC099850.3 siRNA was dissolved in 20 μL of DEPC water and mixed with different volumes of 1 mg/mL SF@PP NPs (containing SF). An excess amount of DEPC water was added to achieve a final reaction volume of 100 μL. The mixture was vortexed for 15 s and incubated at room temperature for 30 min. The optimal mass ratio of siRNA to SF@PP NPs (1:4) was determined using agarose gel electrophoresis. The original AC&SF@PP NPs solution was stored in 4 °C DEPC water for further use [28].

Preparation of CC@AC&SF@PP NPs
For the preparation of CC@AC&SF@PP NPs, the obtained AC&SF@PP NPs were added dropwise to CMCS solutions with different concentrations and stored at room temperature for 30 min. The optimal mass ratio of mPEG5K-PAE10K/SF/AC099850.3 siRNA/CMCS was determined to be 40:4:1:1. The solution of CC@AC&SF@PP NPs was stored in 4 °C DEPC water for subsequent use [28].

Characterization of CC@AC&SF@PP NPs
NPs were negatively stained with 2% (w/v) uranyl acetate for characterization. The morphology of CC@AC&SF@PP NPs was examined using JEM-2100F transmission electron microscopy (TEM) at Qingdao FeiYoute Laboratory. The absorption spectra were recorded using a UV–Vis spectrophotometer from China AOE Instrumentation. The average hydrodynamic diameter distribution and zeta potential were determined using a Zetasizer Nano ZS90 particle analyzer from Malvern [28].

In vitro drug release study
The release behavior of SF from CC@AC&SF@PP NPs was investigated in PBS at pH 7.4 and pH 6.5, respectively, at 37 °C. A 1 mL solution of CC@AC&SF@PP NPs (SF concentration: 0.1 mg/mL) was transferred to a 14 kDa MWCO dialysis bag (Shanghai Maokang Biotechnology Co., Ltd., MP1719-5 M). The dialysis bag was securely tied with cotton thread and immersed in 13 mL of pH 7.4 or pH 6.5 PBS (1% v/v Tween-80 was added to the PBS solution to enhance the dispersion of SF). The temperature was maintained at 37 °C with continuous shaking (150 rpm). At specific time intervals (i.e., 0, 1, 2, 4, 8, 12, 24, 48, 60, 72 h), 500 μL of the release medium was withdrawn and replaced with an equal volume of fresh PBS. The drug release rate was determined using high-performance liquid chromatography [28]. The release experiments were conducted in triplicate, and the results were reported as the mean data.

In vitro drug release study
The release behavior of SF from CC@AC&SF@PP NPs was investigated in PBS at pH 7.4 and pH 6.5, respectively, at 37 °C. The pH 6.5 condition was chosen to mimic the slightly acidic environment of the tumor microenvironment, enhancing the relevance of the drug release and cellular uptake experiments.

In vitro cell uptake assay
HepG2 2.2.15 cells were seeded in a 6-well cell culture plate at a density of 1×10^6 cells/well and incubated overnight in a fresh culture medium. The cells were washed three times with PBS buffer and resuspended in 1 mL of opti-MEM medium. Then, 10 μL of Cy3-AC099850.3 siRNA (20 μM, complexed with Lipo2000) or CC@AC&SF@PP NPs (equivalent amount of siRNA, incubated at pH 6.5 or 7.4) were added to the cells, with each group performed in triplicate. The plates were incubated at 4 °C for 6 h to avoid nonspecific adsorption. The cells were washed three times with PBS and subjected to fluorescence imaging analysis [28].

HBV-HCC in situ tumor model
Male NOD-SCID mice (6 weeks old, weighing 18–22 g) were purchased from Spbf Biotechnology Co., Ltd. (Beijing). All mice were housed in a controlled environment barrier facility with a 12-h light/dark cycle, temperature (24 ± 1 °C), and humidity ($50 \pm 10\%$), and had ad libitum access to food and water [76]. Male NOD-SCID mice were anesthetized by inhalation of isoflurane using a small animal anesthesia machine. After disinfection, the abdomen was opened at the midline, and the median lobe of the liver was exposed. Then, 1×10^6 HepG2 2.2.15

He *et al. Journal of Translational Medicine*   (2024) 22:809

Page 22 of 26

cells dissolved in 50 μL PBS were injected into the liver. The median lobe of the liver was gently reinserted into the abdominal cavity, and the incision was closed layer by layer, followed by disinfection with iodine tincture. After anesthesia recovery, the mice were returned to their original housing environment for approximately 1 week. Tumor-bearing mice were randomly divided into six groups: PBS group, CC@PP group, CC@AC@PP group, CC@NC&SF@PP group, CC@AC&SF@PP group, and AC&SF group (n = 5 per group). Different materials (100 μL) were intravenously injected on days 1, 4, 7, 10, and 13, with an siRNA dose of 2.5 mg/kg and an SF dose of 10 mg/kg. One day after injection, a solution of D-luciferin potassium salt (HY-12591B, MCE) at a concentration of 15 mg/mL was injected intraperitoneally (150 μL), and the anesthetized mice were placed in a bioluminescence imaging system. The imaging system detected the light signal produced by tumor cells and quantified the tumor size. Mice were euthanized 3 days after the last drug injection, and subsequent experiments were conducted using whole liver samples [28].

In vivo tumor uptake assay

For in vivo fluorescence imaging, a partial volume of 100 μL of Cy5-AC099850.3 siRNA or CC@AC&SF@PP NPs (siRNA concentration of 0.5 mg/mL) was intravenously injected into tumor-bearing BALB/c mice. Six hours after injection, we obtained fluorescence images using a small animal in vivo imaging system (CLS136340, IVIS Lumina XRMS). Following anesthesia with isoflurane, we exposed the internal organs of the mice for contrast imaging. After imaging, we retrieved major organs such as lungs, hearts, kidneys, livers, and spleens and imaged them on the same imaging system.

To analyze the distribution of the drug in the tumor of the mice, we embedded the tumor tissue in an optimal cutting temperature compound (OCT). Tumor tissue sections were obtained using an RWD Minux FS800 and mounted on glass slides. Subsequently, the sections were fixed in 4% paraformaldehyde for 15 min and stained with a 10 μg/mL Hoechst 33,258 solution for nuclear staining for 10 min. The sections were then washed with PBS, and fluorescence images were acquired using a confocal microscopy system [28].

Immunohistochemical staining

Tumor tissues from mice were obtained and fixed, followed by decalcification. The samples were then dehydrated using a graded ethanol series and embedded in paraffin. Subsequently, 5 μm thick sections were cut. The sections were baked at 60 °C for 20 min and then sequentially immersed in xylene solution, with each immersion lasting 15 min and xylene solution being replaced in between. After dehydration in anhydrous ethanol for 5 min, further dehydration was performed in a graded ethanol series (70% and 95%) for 10 min each.

To block endogenous peroxidase activity, each section was treated with 3% H_2O_2 at room temperature for 10 min. Citrate buffer was added, and the sections were microwaved for 3 min. After that, the sections were incubated at room temperature for 10 min with an antigen retrieval solution, followed by washing them with PBS three times. Normal goat serum-blocking solution was then applied to the tissue sections, which were subsequently incubated at room temperature for 20 min. A primary antibody, Anti-CD276 antibody (ab219648, 1:4000, Abcam, UK), was added to the sections and incubated overnight at 4 °C.

The next day, a goat anti-rabbit IgG secondary antibody (ab6721, 1:1000) was added and incubated for 30 min. SABC (SA0041, Solarbio) was then added and kept at 37 °C for 30 min. DAB chromogenic reagent (DA1010, Solarbio) was added to the sections and incubated for 6 min. Subsequently, the sections were counterstained with hematoxylin for 30 s. Dehydration was performed using graded ethanol series (70%, 80%, 90%, and 95%) and anhydrous ethanol for 2 min each. Finally, the sections were cleared twice with xylene for 5 min each before being mounted with neutral resin and observed under a light microscope (BX63, Olympus, Japan). The experiment was performed in triplicate. PBS was used instead of the primary antibody as a negative control.

For quantitative analysis, five different fields of view containing immunohistochemistry (IHC) images were selected. The number of cells with brown staining signals in the cytoplasm was counted as positive stained cells, and the total number of cells in each field was also recorded. The percentage of positive cells was calculated as the number of positive stained cells divided by the total number of cells and multiplied by 100% [77].

RT-qPCR

Total RNA was extracted from tissues and cells using Thermo Fisher's Tissue RNA Extraction Kit (12183018A) and Cell RNA Extraction Kit (12183020), respectively, following the standard protocol provided. Subsequently, 1 μg of total RNA was reverse transcribed into cDNA using Fermentas' First Strand cDNA Synthesis Kit (K1622). The synthesized cDNA was then subjected to RT-qPCR analysis using Applied Biosystems' Fast SYBR Green PCR Kit and ABI PRISM 7500 RT-PCR System, with three replicates per well. The relative expression levels of mRNA were calculated using the $2^{-\Delta\Delta Ct}$ method, where $\Delta\Delta Ct$ = (average Ct value of target gene in experimental group—average Ct value of reference gene in experimental group)—(average Ct value of target gene in

control group—average Ct value of reference gene in control group). GAPDH was used as the reference gene. The RT-qPCR reactions were performed in an Applied Biosystems StepOnePlus instrument, with reaction conditions consisting of one cycle at 95 ℃ for 15 min, followed by 40 cycles, each comprising 10 s at 95 ℃ and 60 s at 60 ℃ [68]. For primer sequences, please refer to Table S7. The required reagents and consumables for these experiments were purchased from Wuhan Sibaire Biotechnology Co., Ltd.

Western blot analysis

Proteins were extracted from mouse tumor tissue and HepG2.2.15 cells using the Solarbio Tissue Protein Extraction Kit (EX2171) and Cell Protein Extraction Kit (EX2170), respectively. The protein concentration was determined using the Sigma BCA Protein Assay Kit (BCA1-1KT). Equal amounts of protein (20 μg per lane) were subjected to 10–12% SDS-PAGE electrophoresis. Following electrophoresis, the proteins were transferred to polyvinylidene fluoride (PVDF) membranes from EMD Millipore. The membranes were then blocked with 5% BSA for 2 h, washed with PBS, and incubated overnight at 4℃ with primary antibodies (details of primary antibody manufacturers can be found in Table S8). The primary antibodies used were anti-GAPDH antibody (ab9485, 1:2500) and anti-CD276 antibody (ab105922, 1:1000) provided by Abcam. Subsequently, the membrane was incubated with a secondary antibody, goat anti-rabbit horseradish peroxidase-conjugated antibody (ab6721, 1:2000), from Abcam at room temperature for 2 h after washing. Visualization was done using the enhanced chemiluminescence system (iBright FL1500) from Thermo Fisher. The experiment was repeated three times. The experiments were repeated three times.

Statistical analysis

Data were analyzed using SPSS 21.0 (SPSS, Inc., Chicago, IL, USA). Numerical data are presented as mean ± standard deviation. Independent sample t-tests were used for comparisons between two groups, while one-way analysis of variance (ANOVA) was used for comparisons among multiple groups. Categorical data are presented as proportions or percentages, and comparisons were performed using the Chi-square test. A significance level of $P < 0.05$ was considered statistically significant.

Supplementary Information

The online version contains supplementary material available at https://doi.org/10.1186/s12967-024-05576-y.

Additional file 1: Figure S1. Construction process of HBV-HCC prognostic model: WGCNA analysis, Lasso regression analysis, and survival analysis.Dendrogram of clustering analysis performed by WGCNA on all samples;Scale-free fitting index and average connectivity analysis for different soft thresholds;WGCNA analysis divides genes into different gene modules and provides clustering results;Cross-validation plot of Lasso regression analysis;Kaplan–Meier survival curve for high-risk and low-risk groups based on training set;Kaplan–Meier survival curve for high-risk and low-risk groups based on testing set.

Additional file 2: Figure S2. ROC curve analysis and survival status analysis during the construction process of the HBV-HCC prognostic model. ROC curve analysis based on the training set to evaluate the predictive value of the high-risk and low-risk groups in HBV-HCC diagnosis;ROC curve analysis based on the testing set to evaluate the predictive value of the high-risk and low-risk groups in HBV-HCC diagnosis;Risk curve and patient survival status for the high-risk and low-risk groups based on the training set;Heatmap showing the expression of the six model genes in the high-risk and low-risk groups based on the training set;Risk curve and patient survival status for the high-risk and low-risk groups based on the testing set;Heatmap showing the expression of the six model genes in the high-risk and low-risk groups based on the testing set; High-risk group in the training set: 11 samples; Low-risk group in the training set: 9 samples; High-risk group in the testing set: 12 samples; Low-risk group in the testing set: 12 samples.

Additional file 3: Figure S3. Analysis of the expression levels of model genes and their correlation with immune cells.Differential levels of gene AC012313.9 between 50 normal samples and 44 HBV-HCC samples, AC012313.9, MIR210HG, AL645933.2, C6orf223, GDF10;Correlation analysis between significantly different immune cell components and the expression levels of AC099850.3, with AC099850.3 expression on the x-axis and immune cell content on the y-axis, Dendritic cells resting, T cells follicular helper, and T cells gamma delta;Scatter plot showing the correlation between AC099850.3 and tumor mutation burden; "ns" indicates no significant difference between the groups compared; ** indicates a comparison between the groups with a P value < 0.01; *** indicates a comparison between the groups with a P value < 0.001.

Additional file 4: Figure S4. A scatter plot shows the top 6 genes ranked by correlation with AC099850.3.

Additional file 5: Figure S5. In vivo tumor uptake test and toxicity evaluation of NPs.Bioluminescence and Cy5 fluorescence images of mice in each group;Composite images of organs from mice in each group, with white dashed lines indicating the direction and approximate location of the slices;Fluorescence images of tumor slices from mice in each group;Histological analysis of heart, liver, spleen, lung, and kidney tissues from mice in each group; N = 5.

Additional file 6.

Availability of data and materials
Anonymized data and code used in conducting the analyses will be made available upon request directed to the corresponding author.

He *et al. Journal of Translational Medicine*   (2024) 22:809

Page 24 of 26

Declarations

Ethics approval and consent to participate
All animal experiments were approved by the Animal Ethics Committee of The Second Affiliated Hospital of Nanchang University.

Consent for publication
Not applicable.

Competing interests
The author declares no conflict of interest.

Author details
[1]Department of General Surgery, The Second Affiliated Hospital, Jiangxi Medical College, Nanchang University, No. 1, Minde Road, Nanchang 330006, China. [2]Department of Emergency, The Second Affiliated Hospital, Jiangxi Medical College, Nanchang University, Nanchang 330006, China. [3]Department of Hematology, The Second Affiliated Hospital, Jiangxi Medical College, Nanchang University, Nanchang 330006, China. [4]Department of Gastroenterology, The Second Affiliated Hospital, Jiangxi Medical College, Nanchang University, Nanchang 330006, China.

References
1. Rizzo GEM, Cabibbo G, Craxì A. Hepatitis B virus-associated hepatocellular carcinoma. Viruses. 2022;14(5):986. https://doi.org/10.3390/v14050986.
2. You M, Gao Y, Fu J, et al. Epigenetic regulation of HBV-specific tumor-infiltrating T cells in HBV-related HCC. Hepatology. 2023;78(3):943–58. https://doi.org/10.1097/HEP.0000000000000369.
3. Li YT, Wu HL, Liu CJ. Molecular mechanisms and animal models of HBV-related hepatocellular carcinoma: with emphasis on metastatic tumor antigen 1. Int J Mol Sci. 2021;22(17):9380. https://doi.org/10.3390/ijms22179380.
4. Zhou J, Zhang M, Dong H, et al. Comprehensive analysis of acetylation-related lncRNAs and identified AC099850.3 as prognostic biomarker in non-small cell lung cancer. J Oncol. 2021;2021:4405697. https://doi.org/10.1155/2021/4405697.
5. Chen X, Guo J, Zhou F, et al. Over-expression of long non-coding RNA-AC099850.3 correlates with tumor progression and poor prognosis in lung adenocarcinoma. Front Oncol. 2022;12:895708. https://doi.org/10.3389/fonc.2022.895708.
6. Yue G, Tang J, Zhang L, Niu H, Li H, Luo S. CD276 suppresses CAR-T cell function by promoting tumor cell glycolysis in esophageal squamous cell carcinoma. J Gastrointest Oncol. 2021;12(1):38–51. https://doi.org/10.21037/jgo-21-50.
7. Liu S, Liang J, Liu Z, et al. The role of CD276 in cancers. Front Oncol. 2021;11: 654684. https://doi.org/10.3389/fonc.2021.654684.
8. Zhou WT, Jin WL. B7-H3/CD276: an emerging cancer immunotherapy. Front Immunol. 2021;12: 701006. https://doi.org/10.3389/fimmu.2021.701006.
9. Garbayo E, Pascual-Gil S, Rodriguez-Nogales C, Saludas L, Estella-Hermosode Mendoza A, Blanco-Prieto MJ. Nanomedicine and drug delivery systems in cancer and regenerative medicine. Wiley Interdiscip Rev Nanomed Nanobiotechnol. 2020;12(5):e1637. https://doi.org/10.1002/wnan.1637.
10. Kumagai M. Rinsho Byori. 1987;35(2):161–166.
11. Li Z, Xiao C, Yong T, Li Z, Gan L, Yang X. Influence of nanomedicine mechanical properties on tumor targeting delivery. Chem Soc Rev. 2020;49(8):2273–90. https://doi.org/10.1039/c9cs00575g.
12. Snipstad S, Vikedal K, Maardalen M, Kurbatskaya A, Sulheim E, Davies CL. Ultrasound and microbubbles to beat barriers in tumors: Improving delivery of nanomedicine. Adv Drug Deliv Rev. 2021;177: 113847. https://doi.org/10.1016/j.addr.2021.113847.
13. Pearce AK, O'Reilly RK. Insights into active targeting of nanoparticles in drug delivery: advances in clinical studies and design considerations for cancer nanomedicine. Bioconjug Chem. 2019;30(9):2300–11. https://doi.org/10.1021/acs.bioconjchem.9b00456.
14. Patra JK, Das G, Fraceto LF, et al. Nano based drug delivery systems: recent developments and future prospects. J Nanobiotechnol. 2018;16(1):71. https://doi.org/10.1186/s12951-018-0392-8.
15. Singh S. Nanomedicine-nanoscale drugs and delivery systems. J Nanosci Nanotechnol. 2010;10(12):7906–18. https://doi.org/10.1166/jnn.2010.3617.
16. Zhong F, Liu S, Hu D, Chen L. LncRNA AC099850.3 promotes hepatocellular carcinoma proliferation and invasion through PRR11/PI3K/AKT axis and is associated with patients prognosis. J Cancer. 2022;13(3):1048–60. https://doi.org/10.7150/jca.66092.
17. Cheng Z, Han J, Jiang F, Chen W, Ma X. Prognostic pyroptosis-related lncRNA signature predicts the efficacy of immunotherapy in hepatocellular carcinoma. Biochem Biophys Rep. 2022;32:101389. https://doi.org/10.1016/j.bbrep.2022.101389.
18. Wu F, Wei H, Liu G, Zhang Y. Bioinformatics profiling of five immune-related lncRNAs for a prognostic model of hepatocellular carcinoma. Front Oncol. 2021;11:667904. https://doi.org/10.3389/fonc.2021.667904.
19. Li N, Shen J, Qiao X, Gao Y, Su HB, Zhang S. Long non-coding RNA signatures associated with ferroptosis predict prognosis in colorectal cancer. Int J Gen Med. 2022;15:33–43. https://doi.org/10.2147/IJGM.S331378.
20. Wang Q, Fang Q, Huang Y, Zhou J, Liu M. Identification of a novel prognostic signature for HCC and analysis of costimulatory molecule-related lncRNA AC099850.3. Sci Rep. 2022;12(1):9954. https://doi.org/10.1038/s41598-022-13792-z.
21. Pinyol R, Montal R, Bassaganyas L, et al. Molecular predictors of prevention of recurrence in HCC with sorafenib as adjuvant treatment and prognostic factors in the phase 3 STORM trial. Gut. 2019;68(6):1065–75. https://doi.org/10.1136/gutjnl-2018-316408.
22. Koeberle D, Dufour JF, Demeter G, et al. Sorafenib with or without everolimus in patients with advanced hepatocellular carcinoma (HCC): a randomized multicenter, multinational phase II trial (SAKK 77/08 and SASL 29). Ann Oncol. 2016;27(5):856–61. https://doi.org/10.1093/annonc/mdw054.
23. Bondì ML, Scala A, Sortino G, et al. Nanoassemblies based on supramolecular complexes of nonionic amphiphilic cyclodextrin and sorafenib as effective weapons to kill human HCC cells. Biomacromol. 2015;16(12):3784–91. https://doi.org/10.1021/acs.biomac.5b01082.
24. So YJ, Frentzas S, Segelov E. Is there a place for Ramucirumab after Sorafenib in patients with advanced HCC? Hepatobiliary Surg Nutr. 2019;8(5):546–8. https://doi.org/10.21037/hbsn.2019.04.14.
25. Younis MA, Khalil IA, Elewa YHA, Kon Y, Harashima H. Ultra-small lipid nanoparticles encapsulating sorafenib and midkine-siRNA selectively-eradicate sorafenib-resistant hepatocellular carcinoma in vivo. J Control Release. 2021;331:335–49. https://doi.org/10.1016/j.jconrel.2021.01.021.
26. de Jong YP, Herzog RW. Liver gene therapy and hepatocellular carcinoma: a complex web. Mol Ther. 2021;29(4):1353–4. https://doi.org/10.1016/j.ymthe.2021.03.009.
27. Angelici B, Shen L, Schreiber J, Abraham A, Benenson Y. An AAV gene therapy computes over multiple cellular inputs to enable precise targeting of multifocal hepatocellular carcinoma in mice. Sci Transl Med. 2021;13(624):eabh4456. https://doi.org/10.1126/scitranslmed.abh4456.
28. Song C, Zhang J, Wen R, et al. Improved anti-hepatocellular carcinoma effect by enhanced Co-delivery of Tim-3 siRNA and sorafenib via multiple pH triggered drug-eluting nanoparticles. Mater Today Bio. 2022;16:100350. https://doi.org/10.1016/j.mtbio.2022.100350.
29. Tan Y, Xu Q, Wu Z, et al. Overexpression of PD-L1 is an independent predictor for recurrence in HCC patients who receive sorafenib treatment after surgical resection. Front Oncol. 2022;11:783335. https://doi.org/10.3389/fonc.2021.783335.
30. Chu PY, Chan SH. Cure the incurable? Recent breakthroughs in immune checkpoint blockade for hepatocellular carcinoma. Cancers (Basel). 2021;13(21):5295. https://doi.org/10.3390/cancers13215295.
31. Zhang F, Cai J, Hu K, et al. An immune-related gene signature predicting prognosis and immunotherapy response in hepatocellular carcinoma. Comb Chem High Throughput Screen. 2022;25(13):2203–16. https://doi.org/10.2174/1386207325666220304115006.
32. Fu M, Wang Q, Wang H, et al. Immune-related genes are prognostic markers for prostate cancer recurrence. Front Genet. 2021;12:639642. https://doi.org/10.3389/fgene.2021.639642.

He *et al. Journal of Translational Medicine*   (2024) 22:809

Page 25 of 26

33. Li L, Xia S, Shi X, Chen X, Shang D. The novel immune-related genes predict the prognosis of patients with hepatocellular carcinoma. Sci Rep. 2021;11(1):10728. https://doi.org/10.1038/s41598-021-89747-7.

34. Wu YJ, Liu S, Tian YQ, Fan ZJ, Zhang L, Liu SY. Screening and validation of pivotal genes in hepatitis B virus-associated hepatocellular carcinoma. Zhonghua Gan Zang Bing Za Zhi. 2023;31(8):869–76. https://doi.org/10.3760/cma.j.cn501113-20220420-00213.

35. Bao J, Wu Y, Zhang K, Qi H. AC099850.3/NCAPG axis predicts poor prognosis and is associated with resistance to EGFR tyrosine-kinase inhibitors in lung adenocarcinoma. Int J Gen Med. 2022;15:6917–30. https://doi.org/10.2147/IJGM.S365695.

36. Zhang W, Fang D, Li S, Bao X, Jiang L, Sun X. Construction and validation of a novel ferroptosis-related lncRNA signature to predict prognosis in colorectal cancer patients. Front Genet. 2021;12:709329. https://doi.org/10.3389/fgene.2021.709329.

37. Lu J, An SG, Ma JJ, et al. Topoisomerase IIα gene as a marker for prognostic prediction of hepatocellular carcinoma: a bioinformatics analysis. Chin Med Sci J. 2022;37(4):331–9. https://doi.org/10.24920/004006.

38. Tang XY, Luo ZL, Xiong YL, et al. The proliferative role of immune checkpoints in tumors: double regulation. Cancers (Basel). 2022;14(21):5374. https://doi.org/10.3390/cancers14215374.

39. Li R, Zatloukalova P, Muller P, et al. The MDM2 ligand Nutlin-3 differentially alters expression of the immune blockade receptors PD-L1 and CD276. Cell Mol Biol Lett. 2020;25:41. https://doi.org/10.1186/s11658-020-00233-w.

40. Liu Y, Veeraraghavan V, Pinkerton M, et al. Viral biomarkers for hepatitis B virus-related hepatocellular carcinoma occurrence and recurrence. Front Microbiol. 2021;12:665201. https://doi.org/10.3389/fmicb.2021.665201.

41. Qu S, Jin L, Huang H, Lin J, Gao W, Zeng Z. A positive-feedback loop between HBx and ALKBH5 promotes hepatocellular carcinogenesis. BMC Cancer. 2021;21(1):686. https://doi.org/10.1186/s12885-021-08449-5.

42. Shi M, Li YY, Xu RN, et al. Mesenchymal stem cell therapy in decompensated liver cirrhosis: a long-term follow-up analysis of the randomized controlled clinical trial. Hepatol Int. 2021;15(6):1431–41. https://doi.org/10.1007/s12072-021-10199-2.

43. Zhang L, Chen J, Jiang H, et al. MR elastography as a biomarker for prediction of early and late recurrence in HBV-related hepatocellular carcinoma patients before hepatectomy. Eur J Radiol. 2022;152: 110340. https://doi.org/10.1016/j.ejrad.2022.110340.

44. Magrin L, Fanale D, Brando C, et al. POLE, POLD1, and NTHL1: the last but not the least hereditary cancer-predisposing genes. Oncogene. 2021;40(40):5893–901. https://doi.org/10.1038/s41388-021-01984-2.

45. Tian Y, Ma J, Jing X, et al. Radiation therapy for extensive-stage small-cell lung cancer in the era of immunotherapy. Cancer Lett. 2022;541: 215719. https://doi.org/10.1016/j.canlet.2022.215719.

46. Simó-Perdigó M, Vercher-Conejero JL, Viteri S, García-Velloso MJ. Immunotherapy, cancer and PET. Inmunoterapia, cáncer y PET. Rev Esp Med Nucl Imagen Mol (Engl Ed). 2021;40(2):123–35. https://doi.org/10.1016/j.remn.2021.02.001.

47. Meng F, Zhao J, Tan AT, et al. Immunotherapy of HBV-related advanced hepatocellular carcinoma with short-term HBV-specific TCR expressed T cells: results of dose escalation, phase I trial. Hepatol Int. 2021;15(6):1402–12. https://doi.org/10.1007/s12072-021-10250-2.

48. Zhang J, Hu C, Xie X, Qi L, Li C, Li S. Immune checkpoint inhibitors in HBV-caused hepatocellular carcinoma therapy. Vaccines (Basel). 2023;11(3):614. https://doi.org/10.3390/vaccines11030614.

49. Shao D, Li Y, Wu J, et al. An m6A/m5C/m1A/m7G-related long non-coding RNA signature to predict prognosis and immune features of glioma. Front Genet. 2022;13:903117. https://doi.org/10.3389/fgene.2022.903117.

50. Liu P, Zhou L, Chen H, He Y, Li G, Hu K. Identification of a novel intermittent hypoxia-related prognostic lncRNA signature and the ceRNA of lncRNA GSEC/miR-873–3p/EGLN3 regulatory axis in lung adenocarcinoma. PeerJ. 2023;11:e16242. https://doi.org/10.7717/peerj.16242.

51. Zhang Q, Cheng M, Fan Z, Jin Q, Cao P, Zhou G. Identification of cancer cell stemness-associated long noncoding RNAs for predicting prognosis of patients with hepatocellular carcinoma. DNA Cell Biol. 2021;40(8):1087–100. https://doi.org/10.1089/dna.2021.0282.

52. Mahaling B, Baruah N, Ahamad N, Maisha N, Lavik E, Katti DS. A non-invasive nanoparticle-based sustained dual-drug delivery system as an eyedrop for endophthalmitis. Int J Pharm. 2021;606: 120900. https://doi.org/10.1016/j.ijpharm.2021.120900.

53. Cancer Genome Atlas Research Network. Electronic address: wheeler@bcm.edu; Cancer Genome Atlas Research Network. Comprehensive and Integrative Genomic Characterization of Hepatocellular Carcinoma. Cell. 2017;169(7):1327–1341.e23. https://doi.org/10.1016/j.cell.2017.05.046.

54. Gu X, Li S, Ma X, Huang D, Li P. Heterogeneity characterization of hepatocellular carcinoma based on the sensitivity to 5-fluorouracil and development of a prognostic regression model. Front Pharmacol. 2023;14:1252805. https://doi.org/10.3389/fphar.2023.1252805.

55. Li W, Zhao B, Wang Q, Lu J, Wu X, Chen X. Integrated analysis of tumour-derived exosome-related immune genes to predict progression and immune status of hepatocellular carcinoma. Clin Immunol. 2023;256: 109774. https://doi.org/10.1016/j.clim.2023.109774.

56. Lin XH, Li DP, Liu ZY, et al. Six immune-related promising biomarkers may promote hepatocellular carcinoma prognosis: a bioinformatics analysis and experimental validation. Cancer Cell Int. 2023;23(1):52. https://doi.org/10.1186/s12935-023-02888-9.

57. Zheng GL, Zhang GJ, Zhao Y, Zheng ZC. Screening protein prognostic biomarkers for stomach adenocarcinoma based on the cancer proteome atlas. Front Oncol. 2022;12:901182. https://doi.org/10.3389/fonc.2022.901182.

58. Wen YD, Zhu XS, Li DJ, Zhao Q, Cheng Q, Peng Y. Proteomics-based prognostic signature and nomogram construction of hypoxia microenvironment on deteriorating glioblastoma (GBM) pathogenesis. Sci Rep. 2021;11(1):17170. https://doi.org/10.1038/s41598-021-95980-x.

59. Zheng H, Liu H, Li H, Dou W, Wang X. Weighted gene co-expression network analysis identifies a cancer-associated fibroblast signature for predicting prognosis and therapeutic responses in gastric cancer. Front Mol Biosci. 2021;8:744677. https://doi.org/10.3389/fmolb.2021.744677.

60. Tao C, Huang K, Shi J, Hu Q, Li K, Zhu X. Genomics and prognosis analysis of epithelial-mesenchymal transition in glioma. Front Oncol. 2020;10:183. https://doi.org/10.3389/fonc.2020.00183.

61. Jiang L, Zhang M, Wu J, et al. Exploring diagnostic m6A regulators in endometriosis. Aging (Albany NY). 2020;12(24):25916–38. https://doi.org/10.18632/aging.202163.

62. Newman AM, Liu CL, Green MR, et al. Robust enumeration of cell subsets from tissue expression profiles. Nat Methods. 2015;12(5):453–7. https://doi.org/10.1038/nmeth.3337.

63. Ali HR, Chlon L, Pharoah PD, Markowetz F, Caldas C. Patterns of Immune infiltration in breast cancer and their clinical implications: a gene-expression-based retrospective study. PLoS Med. 2016;13(12):e1002194. https://doi.org/10.1371/journal.pmed.1002194.

64. Kan A, Liu S, He M, et al. MZF1 promotes tumour progression and resistance to anti-PD-L1 antibody treatment in hepatocellular carcinoma. JHEP Rep. 2023;6(1):100939. https://doi.org/10.1016/j.jhepr.2023.100939.

65. Zhu Y, Tan JK, Goon JA. Cuproptosis- and m6A-related lncRNAs for prognosis of hepatocellular carcinoma. Biology (Basel). 2023;12(8):1101. https://doi.org/10.3390/biology12081101.

66. Du Y, Miao W, Jiang X, et al. The epithelial to mesenchymal transition related gene calumenin is an adverse prognostic factor of bladder cancer correlated with tumor microenvironment remodeling, gene mutation, and ferroptosis [published correction appears in Front Oncol. 2023 May 11;13:1185029. 10.3389/fonc.2023.1185029]. Front Oncol. 2021;11:683951. https://doi.org/10.3389/fonc.2021.683951.

67. He H, Zhou J, Cheng F, Li H, Quan Y. MiR-3677-3p promotes development and sorafenib resistance of hepatitis B-related hepatocellular carcinoma by inhibiting FOXM1 ubiquitination. Hum Cell. 2023;36(5):1773–89. https://doi.org/10.1007/s13577-023-00945-z.

68. Zhao K, Zhang Y, Kang L, et al. Methylation of microRNA-129–5P modulates nucleus pulposus cell autophagy by targeting Beclin-1 in intervertebral disc degeneration. Oncotarget. 2017;8(49):86264–76. https://doi.org/10.18632/oncotarget.21137.

69. Gao W, Shen R. Nanogel enhances the efficacy of MLN8237 in treating hepatocellular carcinoma. J Biomater Appl. 2023;38(4):527–37. https://doi.org/10.1177/08853282231202326.

70. Zhu G, Cheng Z, Huang Y, et al. MyD88 mediates colorectal cancer cell proliferation, migration and invasion via NF-κB/AP-1 signaling pathway. Int J Mol Med. 2020;45(1):131–40. https://doi.org/10.3892/ijmm.2019.4390.

71. Liu P, Jia SB, Shi JM, et al. LncRNA-MALAT1 promotes neovascularization in diabetic retinopathy through regulating miR-125b/VE-cadherin

He *et al. Journal of Translational Medicine*   (2024) 22:809

Page 26 of 26

axis. Biosci Rep. 2019;39(5):BSR20181469. https://doi.org/10.1042/BSR20 181469.

72. Liu R, Guo H, Lu S. MiR-335-5p restores cisplatin sensitivity in ovarian cancer cells through targeting BCL2L2. Cancer Med. 2018;7(9):4598–609. https://doi.org/10.1002/cam4.1682.

73. Pan X, Hong X, Li S, Meng P, Xiao F. METTL3 promotes adriamycin resistance in MCF-7 breast cancer cells by accelerating pri-microRNA-221-3p maturation in a m6A-dependent manner. Exp Mol Med. 2021;53(1):91– 102. https://doi.org/10.1038/s12276-020-00510-w.

74. Saraswati S, Alhaider A, Abdelgadir AM, Tanwer P, Korashy HM. Phloretin attenuates STAT-3 activity and overcomes sorafenib resistance targeting SHP-1-mediated inhibition of STAT3 and Akt/VEGFR2 pathway in hepatocellular carcinoma. Cell Commun Signal. 2019;17(1):127. https://doi.org/10.1186/s12964-019-0430-7.

75. Ke M, Zhang Z, Xu B, et al. Baicalein and baicalin promote antitumor immunity by suppressing PD-L1 expression in hepatocellular carcinoma cells. Int Immunopharmacol. 2019;75: 105824. https://doi.org/10.1016/j.intimp.2019.105824.

76. Maranda G, Gagnon D. Les blessures par arme à feu: évaluation et traitement [Gunshot wounds: evaluation and treatment]. J Dent Que. 1987;24:337–40.

77. Wang X, Wu Y. Protective effects of autophagy inhibitor 3-methyladenine on ischemia-reperfusion-induced retinal injury. Int Ophthalmol. 2020;40(5):1095–101. https://doi.org/10.1007/s10792-019-01272-9.

Publisher's Note

Springer Nature remains neutral with regard to jurisdictional claims in published maps and institutional affiliations.